



Comets in Context: Comparing Comet Compositions with Protosolar Nebula Models

Karen Willacy¹ , Neal Turner¹ , Boncho Bonev² , Erika Gibb³ , Neil Dello Russo⁴ , Michael DiSanti^{5,6} ,
Ronald J. Vervack Jr.⁴ , and Nathan X. Roth^{7,8}

¹ Jet Propulsion Laboratory, California Institute of Technology, MS 169-506, 4800 Oak Grove Drive Pasadena, CA 91109, USA

² Department of Physics, American University, Washington D.C., USA

³ Department of Physics and Astronomy, University of Missouri-St Louis, St Louis, MO, USA

⁴ Johns Hopkins Applied Physics Laboratory, 11100 Johns Hopkins Road, Laurel, MD 20723, USA

⁵ Solar System Exploration Division, Planetary Science Laboratory Code 693, NASA/Goddard Space Flight Center, Greenbelt, MD, USA

⁶ Goddard Center for Astrobiology, NASA/Goddard Space Flight Center, Greenbelt, MD, USA

⁷ Solar System Exploration Division, Astrochemistry Laboratory Code 691, NASA Goddard Space Flight Center, 8800 Greenbelt Road, Greenbelt, MD 20771, USA

⁸ Department of Physics, The Catholic University of America, 620 Michigan Avenue N.E., Washington, DC 20064, USA

Received 2021 May 24; revised 2022 April 11; accepted 2022 April 14; published 2022 June 7

Abstract

Comets provide a valuable window into the chemical and physical conditions at the time of their formation in the young solar system. We seek insights into where and when these objects formed by comparing the range of abundances observed for nine molecules and their average values across a sample of 29 comets to the predicted midplane ice abundances from models of the protosolar nebula. Our fiducial model, where ices are inherited from the interstellar medium, can account for the observed mixing ratio ranges of each molecule considered, but no single location or time reproduces the abundances of all molecules simultaneously. This suggests that each comet consists of material processed under a range of conditions. In contrast, a model where the initial composition of disk material is “reset,” wiping out any previous chemical history, cannot account for the complete range of abundances observed in comets. Using toy models that combine material processed under different thermal conditions, we find that a combination of warm (CO-poor) and cold (CO-rich) material is required to account for both the average properties of the Jupiter-family and Oort cloud comets, and the individual comets we consider. This could occur by the transport (either radial or vertical) of ice-coated dust grains in the early solar system. Comparison of the models to the average Jupiter-family and Oort cloud comet compositions suggests the two families formed in overlapping regions of the disk, in agreement with the findings of A’Hearn et al. and with the predictions of the Nice model.

Unified Astronomy Thesaurus concepts: [Astrochemistry \(75\)](#); [Comet origins \(2203\)](#); [Interstellar molecules \(849\)](#); [Protoplanetary disks \(1300\)](#); [Solar nebulae \(1508\)](#)

1. Introduction

Comets are among the best-preserved remnants of the early solar system. They are the only class of primitive bodies to retain a rich inventory of volatiles accreted in the cold outer regions of the protosolar nebula. Some molecular evolution may have occurred inside comets since they formed, but despite this, their primitive volatiles and easy accessibility for remote sensing investigations make comets our best path to investigating the conditions in the icy zone of the protosolar nebula during their epoch of formation.

Comets likely formed at diverse distances from the young Sun. The main scenarios for their formation are (a) sequential agglomeration, where two-body collisions build up successively larger masses (Weidenschilling 1977, 1997; Donn 1990; Kataoka et al. 2013), (b) gravitational collapse of a pebble cloud instigated by a mechanism such as the streaming instability (e.g., Youdin & Goodman 2005; Simon et al. 2016), or (c) a combination of the two (Davidsson et al. 2016). Once formed, many nuclei were gravitationally scattered by the young giant planets, sent either to the inner solar system or to their present-day dynamical reservoirs: the Oort Cloud (Oort 1950) and the scattered Kuiper Disk (Gladman 2005).

Dynamical models of the young solar system based on the “Nice model” (Gomes et al. 2005; Tsiganis et al. 2005) suggest these two reservoirs were seeded by comets that formed in overlapping regions, but in as yet unknown proportions. Today, various processes gravitationally perturb individual comets from these reservoirs, sending them to the inner solar system, where sunlight warms the ices leading to the outgassing that enables their compositions to be measured.

Measurements of cometary volatiles have been made with both space probes and ground-based telescopes. EPOXI and Rosetta provided in situ measurements, and a new space mission, Comet Interceptor, is being planned to focus specifically on newly discovered Oort cloud comets (OCCs; Snodgrass & Jones 2019). On the ground, modern near-infrared spectrographs (iSHELL at IRTF, and NIRSPEC-2 at Keck), as well as the submillimeter interferometer at the Atacama Large Millimeter/submillimeter Array, are being used for comet science. The primary motivation and overriding theme for these extensive studies is the need for an improved understanding of comets as relics of the early solar system that retain a rich inventory of volatiles from the cold regions of the protosolar nebula (A’Hearn 2017, and references therein).

Like comet science, chemical modeling of protoplanetary disks (PPDs) is driven by the challenge of understanding the conditions for planetary system formation. (PPDs around other stars are the external equivalent of the protosolar nebula). Modeling the disks’ physical and chemical structure yields



Original content from this work may be used under the terms of the [Creative Commons Attribution 4.0 licence](#). Any further distribution of this work must maintain attribution to the author(s) and the title of the work, journal citation and DOI.

three distinct vertical regions: (1) a cold midplane, where ices freeze onto dust grains, and where comet nuclei eventually form; (2) a warm molecular region, where ices sublime and are then processed via gas-phase reactions involving radicals and ions, produced by the protostellar radiation field; and (3) a hot ionized region containing predominantly atoms and atomic ions (Figure 1 in Bergin et al. 2007). Flows within the disk mix material between the layers, driving further molecular evolution. Historically, models have tended to be focused on interpreting the abundances of gas-phase molecules observed in the atmospheres of the PPDs around young stars, with less emphasis on solid-phase volatiles in the protosolar nebula midplane and their links to comets. This trend has shifted in recent years with new modeling projects tailored specifically to predicting the midplane abundances of volatiles (Furuya & Aikawa 2014; Drozdovskaya et al. 2014, 2016; Willacy et al. 2015; Kamp 2020; Eistrup et al. 2019). Understanding comets’ connections to the early solar system requires combining simulations treating the midplane ice inventory with ongoing efforts to disentangle formative from evolutionary signatures in measured abundances of comet volatiles (Bonev et al. 2014; Gibb et al. 2017).

Here, we investigate the links between disk chemistry and comet composition by modeling the evolution of the molecular abundances in the ices found in the midplane of the solar nebula. This work expands on previous studies by comparing the modeling results with observations of individual comets, as well as the typical composition of comets, considering the ensemble-averaged and range of abundances across the observed objects for each molecule. Diverse orbital and thus solar exposure histories mean that post-formation processing may vary greatly even within each family. We therefore compare the protosolar nebula models to the ensemble properties first. The disk modeling approach is described in Section 2 and the comet observations in Section 3. We discuss the results from three models: the fiducial model (Section 4), a model with a low cosmic-ray ionization rate (Section 5), and a model with atomic (“reset”) input abundances where it is assumed that any molecules formed in the molecular cloud are destroyed during the disk formation (Section 6). In Section 7 we consider whether the comparison between models and observations suggests any systematic differences between Jupiter-family comets (JFCs) and OCCs. In Section 8.1 we attempt to fit the average compositions and those of individual comets in a scenario where most of the comets consist of material from a single place and time. Because this is not possible, in Section 8.2 we examine whether the ensemble and the individual comets could have formed out of ices processed at different locations in the protosolar nebula. We discuss the findings’ ramifications in Section 9 and summarize our conclusions in Section 10.

2. Disk Modeling Approach

2.1. Density and Temperature

The disk’s density and temperature structure is taken from a 1 + 1D model kindly provided by Paula d’Alessio and constructed using the methods set out in d’Alessio et al. (2001). The total mass and its radial distribution are similar to those of the minimum mass solar nebula. The disk orbits a solar-mass star $2.6 R_{\odot}$ in radius with effective temperature 4000 K. Mass accretes from disk to star at a rate $2 \times 10^{-8} M_{\odot} \text{ yr}^{-1}$.

Table 1
Star and Disk Parameters

Parameter	Value
α	0.005
M_*	$1 M_{\odot}$
R_*	$2.6 R_{\odot}$
T_*	4000 K
\dot{M}	$2 \times 10^{-8} M_{\odot} \text{ yr}^{-1}$
a_{\min}	$0.005 \mu\text{m}$
a_{\max}	1 mm

Well-mixed in the disk’s gas are dust particles following a power-law size distribution with index -3.5 between $0.005 \mu\text{m}$ and 1 mm. The temperature is computed by balancing radiative cooling with heating by starlight and by accretion power under the α viscosity prescription of Shakura & Sunyaev (1973). The temperatures of the gas and dust are assumed to be equal inside the disk. Resulting temperatures fall with distance, R , from the star approximately as $R^{-0.5}$. These parameters are summarized in Table 1. The disk’s density and temperature structure remains fixed for the duration of the chemical modeling and does not evolve with time. We evolve the chemical composition on the midplane between 1 au and 35 au. The inner boundary falls just inside the water snowline, and the radial extent covers the likely comet formation zone in the protosolar nebula.

2.2. Chemical Evolution

Our chemical network is a subset of the UMIST database (RATE12; McElroy et al. 2013), expanded to include gas–grain interactions and grain surface reactions. In addition, some reactions from the KIDA database (Wakelam et al. 2012) have been added to extend the sulfur network and the neutral–neutral chemistry in the gas phase (Appendix A). The grain chemistry is calculated using the rate equation method. We use a “two-phase” model, in which the composition of the gas and ice are followed, with the approach described in Cuppen et al. (2017). This modifies the rate equations to take into account the number of ice monolayers on the grains and the competition between reaction, diffusion, and desorption. We assume that the upper four layers of the ice mantle are chemically active and that the size of the barrier to surface diffusion is $0.35 \times$ the binding energy, within the range suggested by the Monte Carlo simulations of Karssemeijer & Cuppen (2014). H and H_2 are allowed to tunnel through any activation barriers.

Ionization is driven by cosmic rays, the cosmic-ray-induced photon field (Prasad & Tarafdar 1983), and the decay of radioactive nuclides. The effect of the stellar and interstellar photon fields are ignored because of they do not penetrate to the midplane. For the cosmic-ray ionization rate (ζ_{CR}), we adopt the approach of Semenov et al. (2004), where cosmic rays enter the disk from both its top and bottom surfaces and are attenuated depending on the surface density:

$$\zeta_{\text{CR}} = 0.5 \zeta_0 [\exp(-\Sigma_1(z, R)/100) + \exp(-\Sigma_2(z, R)/100)] \text{ s}^{-1} \quad (1)$$

where Σ_1 and Σ_2 are the column densities (in g cm^{-2} to the top and bottom of the disk, respectively), and ζ_0 is the interstellar cosmic-ray ionization rate. In our fiducial model, we use the standard interstellar value of $1.3 \times 10^{-17} \text{ s}^{-1}$, whereas in a low-ionization version, we use a value 10 times smaller. The

Table 2
Binding Energies of Important Species

Species	Binding Energy	Species	Binding Energy
H	650	H ₂	500
CH ₄	1250	CO	1100
H ₂ CO	3260	CH ₃ OH	3820
CO ₂	2267	H ₂ O	4800
N ₂	990	NH ₃	2715
OH	3210	O	1660
O ₂	898	C ₂ H ₂	2090
C ₂ H ₆	2183	HCN	1583
HNC	1510	OCS	2325
CH	590		

Note. Values are taken from Table 3 in Penteado et al. (2017).

cosmic-ray photodissociation rates from RATE12 are scaled to account for the change in ζ_{CR} compared to ζ_0 . Ionization due to the decay of radioactive nuclides such as ^{26}Al has a rate given by

$$\zeta_{\text{Al}} = 6.5 \times 10^{-19} \exp(-0.693t/0.73) \text{ s}^{-1} \quad (2)$$

where t is the elapsed time in millions of years. The exponential factor accounts for the decreasing abundance of ^{26}Al as it decays with a half-life of 0.73 Myr (Castillo-Rogez et al. 2009).

Reaction and diffusion rates on the grains depend on the ice species' binding energies on the surface. We use the energies given in Table 2 (and taken from Penteado et al. (2017)). Following Cuppen et al. (2017), only the ice's uppermost four monolayers are available to desorb. We assume molecules are returned to the gas by cosmic-ray heating of the grains and by thermal desorption. In the midplane, the ices are shielded from both interstellar and stellar photons, but cosmic rays still penetrate, and their cascade yields energetic photons that can photodesorb the ices and photodissociate the ice molecules. We assume the latter occurs at the same rate as gas-phase photodissociation (Ruffle & Herbst 2001).

2.3. Initial Abundances

The initial abundances of all chemical species in the fiducial disk model come from a molecular cloud chemistry model. We treat a location in the cloud's interior where the temperature is 10 K, the total hydrogen density is $2 \times 10^4 \text{ cm}^{-3}$, and the visual extinction is 10 magnitudes. We begin the cloud model with all elements in their atomic form except carbon, which is present as C^+ , and hydrogen, which is 1% atomic with the rest molecular (Table 3). The assumed C/O ratio is 0.54, roughly solar. We then evolve the composition for 1 Myr. Table 4 shows the resulting ice abundances alongside the ices observed toward background stars and in low-mass young stars. Overall there is reasonable agreement with both sets of observational data.

It is possible that energetic processing during disk formation could destroy any molecules that formed in the parent molecular cloud. In this case, the disk chemistry would start from ions and atoms rather than molecules. The input composition would be “reset,” wiping out any record of the molecular cloud chemistry. To explore the implications for the results, we compute an additional disk model, starting from such atomic abundances (see Section 6). For this model, the

Table 3
Initial Abundances for the Molecular Cloud Model Given as a Fractional Abundance Relative to Total Hydrogen ($=n(\text{H}) + 2n(\text{H}_2)$)

Species	Fractional Abundance
H	1 (−2)
H ₂	4.95 (−1)
He	1.4 (−1)
C^+	1.3 (−4)
O	2.4 (−4)
N	2.14 (−5)
S^+	1.66 (−5)
Si^+	8.0 (−9)

Note. The C/O ratio is 0.54.

Table 4
Ice Abundances Calculated in the Molecular Cloud Model after 1 Myr

Molecule	Cloud Model	Background Stars	Low-mass YSO
H ₂ O	100	100	100
CO	40.5	9–67	<3–85
CO ₂	4.7	14–43	12–50
CH ₄	13.3	<3	1–11
CH ₃ OH	7.2	<1–12	<1–25
H ₂ CO	10.1	...	~6
OCS	0.02	<0.02	<1.6
NH ₃	4.7	<9	3–10
HCN	3.2
C ₂ H ₂	0.02
C ₂ H ₆	1.8 (−3)

Note. Also shown are the range of observed ice abundances toward background stars and low-mass young stellar objects (YSOs; from Table 2 in Boogert et al. 2015). Abundances are given as a percentage relative to water ice. “...” indicates that no observational data are available.

initial conditions are the same as for the cloud model in Table 3. In reality, a combination of the two scenarios is possible, with some molecules being destroyed and others surviving intact (e.g., Lunine et al. 1991; Neufeld & Hollenbach 1994; Visser et al. 2009). This possibility is not considered here.

3. Comet Sample

Present-day cometary volatiles' composition could be affected by various post-formation processes, short- or long-term. Short-term processes include diurnal and seasonal variations that are highly variable from comet to comet. Long-term processes are expected to depend strongly on a comet's dynamical history. However, there is compelling evidence that the volatiles retain cosmogonic signatures. First, the nucleus of comet 67P/Churyumov-Gerasimenko shows near-solar abundances of oxygen and carbon from in situ measurements (Rubin et al. 2019). Second, the two fragments of the JFC 73P/SW3 have similar compositions, in contrast to the diversity seen in the comet population as a whole (Dello Russo et al. 2007). Similarly, the OCCs Tabur (C/1996 Q1) and Liller (C/1988 A1), thought from their orbits to be fragments of a single parent body, have similar compositions

Table 5
Average Observed Molecular Abundances as a Percentage Relative to Water Taken from Table 3 in DR16

Molecule	OCC			JFC			All Comets Average
	Lower Limit	Average	Upper Limit	Lower Limit	Average	Upper Limit	
CH ₃ OH	<0.2 ^a	2.21	3.72 ^b	0.54 ^c	1.73	3.48 ^d	2.06
HCN	0.07 ^e	0.22	0.50 ^f	0.03 ^g	0.17	0.29 ^c	0.21
NH ₃	0.10 ^h	0.91	3.63 ⁱ	<0.09 ^g	0.59	0.90 ^j	0.80
H ₂ CO	<0.04 ^e	0.33	1.10 ^j	0.13 ^l	0.26	0.84 ^j	0.31
C ₂ H ₂	0.04 ^e	0.16	0.45 ^l	0.03 ^g	0.07	0.15 ^m	0.13
C ₂ H ₆	0.26 ^e	0.63	1.97 ^f	0.12 ⁿ	0.34	0.75 ^k	0.55
CH ₄	0.15 ^a	0.88	1.57 ^f	<0.25 ^o	0.31	0.54 ⁱ	0.78
CO	0.4 ^e	6.1	26.2 ^p	0.3 ^k	1.6	4.3 ⁱ	5.20
OCS	0.04 ^q	0.31	0.41 ^r	0.06 ^d	0.095	0.12 ⁿ	0.17

Note. Data for OCS comes from Saki et al. (2020). The table shows the range of values measured (from lower limit to upper limit) and the average for the class of comets (OCCs and JFCs). Letters indicate to which comet a particular observation refers. Note that these ranges are based on relatively few measurements and so are unlikely to represent the true range in comets. This is especially true where we have very few measurements (e.g., of CH₄ and OCS in JFCs).

References. ^aC/1999 S4, ^bC/2007 N3, ^cSW3-B, ^d2P/Encke, ^e8P/Tuttle, ^fC/2007 W1, ^g6P/d’Arrest, ^hC/2013 R1, ⁱC/2012 S1, ^j9P/Tempel 1, ^k103P/Hartley 2, ^lC/2006 P1, ^m81P/Wild, ⁿ21P/G-Z, ^o73P/SW3-C, ^pC/1995 O1, ^qC/2002 T7, ^rHale-Bopp.

(Turner & Smith 1999). Such fragments would be unlikely to share compositions if the original nucleus suffered depth-dependent processing during its numerous passages around the Sun. Furthermore, a study of product species based on optical measurements of 85 comets shows no correlation between carbon-chain depletion and dynamical age, suggesting the differences in carbon-chain chemistry among at least some of the comets are natal (A’Hearn et al. 1995).

Because the degree of post-formation processing is unknown and will be different for each comet, we use an ensemble average of a sample of comets as the first point of comparison for our protosolar nebula model. The sample includes nine JFCs and 20 OCCs (Appendix B). The observations are taken from Dello Russo et al. (2016, hereafter DR16), with the addition of OCS data from Saki et al. (2020).

The species included in our study are: HCN, NH₃, H₂CO, CH₃OH, C₂H₂, C₂H₆, CH₄, CO, and H₂O (DR16). We also include OCS, whose abundances in several of our comets were recently reported by Saki et al. (2020). This selection of species is motivated, first, by their belonging to different chemical groups (symmetric hydrocarbons, oxygen-carbon compounds, nitrogen-bearing species), as optimal to connect with astrochemical models. OCS is included because it forms a link between the carbon and oxygen chemistry and that of sulfur, and it is one of the few sulfur molecules to have been observed in a sufficient number of comets to allow an average to be determined. Second, the measurements of their relative abundances are based on (1) simultaneous observations of trace volatiles and H₂O, and (2) analysis with the same technique. These two conditions together result in the most reliable relative abundances as needed for comparison with disk models. The list of species does not include CO₂, a major volatile, because it is commonly measured by different techniques and at different times. Interpreting the CO₂ abundances can be a subject of a separate dedicated study.

We consider the mixing ratios averaged over the complete sample of 29 comets, as well as averages for the JFC and OCC subsamples individually (Table 5 and Appendix B). Full details of the observations and the calculation of the average compositions are given in DR16, but to summarize, the averages used are an unweighted mean of the mixing ratios with respect to water of a given species in each comet. Some

Table 6
Summary of Parameters Used in the Modeling

Model	Input Abundances	ζ
fiducial model	“inheritance”	ζ_0
low ionization	“inheritance”	$0.1\zeta_0$
atomic	“reset”	ζ_0

Note. The “inheritance” input abundances indicate that the initial abundances in the disk model are taken from the molecular cloud model described in Section 2.3.

observations (those in parentheses in Appendix B) were excluded from the calculation of the average composition for various reasons, e.g., location of comet when measurements were taken, and poor constraints on the observations (see DR16 for details). The average observed abundance and the upper and lower limits for each molecule are given in Table 5.

While this paper was in review, a new set of measurements was published by Lippi et al. (2021, hereafter L21), including 20 of the comets in the DR16 survey. Although in-depth comparison between the two surveys is outside the scope of this paper, in Appendix C we carefully assess how the new L21 (together with their earlier paper, Lippi et al. 2020, hereafter L20) results affect our analysis. None of the conclusions in this work, as presented in Section 10, are changed by the introduction of the new survey.

Comparing the two families, there are individual JFCs and OCCs with very similar abundances of volatiles. The OCCs show wider ranges in the molecular mixing ratios relative to water, as well as higher average abundances. Every species’ mixing ratio spans a range of at least one order of magnitude. However, we emphasize JFCs are an underrepresented class in compositional studies of all parent species. Currently, they seem more depleted in the hyper-volatiles CO and CH₄ than OCCs, but very few measurements for these species have been feasible in JFCs, due to their weaker intrinsic brightness and Doppler-shift limitations (DiSanti et al. 2017).

4. Fiducial Model Results

In this section we present results from the fiducial protosolar nebula model. Sections 5 and 6, respectively, cover a version where the cosmic-ray ionization rate is reduced by one order of

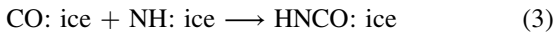
magnitude and a version where the cosmic-ray rate is normal but all molecules except H_2 are initially dissociated, with abundances given in Table 3 (“reset” abundances). Table 6 summarizes the different models. The results are compared to the average values and ranges of the mixing ratios from the complete sample of JFCs and OCCs.

Figure 1 shows the distributions of the ices as predicted by the fiducial model, overlaid with the corresponding abundances observed in the comets. All are shown as percentages of the water ice. All nine molecules under consideration can be accounted for by some combination of time and location in the model disk as follows.

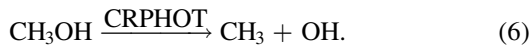
4.1. CO, H_2CO , and CH_3OH

The $\text{CO}/\text{H}_2\text{O}$ mixing ratio in the fiducial disk ranges from 0%–41% depending on time and location. The model matches the entire range of the comet observations in a region close to the CO snowline. The highest value of $\text{CO}/\text{H}_2\text{O}$ observed in our comet sample is in Hale-Bopp. A weighted average value of 26.2% was determined by DR16, and this can be matched by the models around 17 au. The highest individual measurement in this comet is $41\% \pm 13\%$, similar to the molecular cloud model abundance and matched by the disk model at $R > 20$ au.

The CO ice abundance does not increase in the disk model, and the molecular cloud value is maintained until this molecule is destroyed either by reactions or desorption. Thermal desorption produces the CO snowline between 12 and 15 au, whereas the decrease at larger radii after 1 Myr is due to cosmic-ray desorption, dissociation by cosmic-ray-induced photons, and the reactions:



In the molecular cloud, the mixing ratios of CH_3OH and H_2CO are higher than observed in comets. A good fit with the observations is only found after these molecules’ abundances are reduced by processing in the disk. Their destruction occurs mainly by cosmic-ray photons (Figure 2). Although some recycling between H_2CO and CH_3OH occurs, there is a gradual loss of these molecules through



CH_3 then goes on to form CH_4 . The observed range in $\text{CH}_3\text{OH}/\text{H}_2\text{O}$ is matched by the model between 0.3 and 3 Myr. For H_2CO , the fit is over a narrow range of times from 2 to 5 Myr at $R < 20$ au, and between 2 and 60 Myr at $R > 20$ au.

Another way to reduce the abundance of H_2CO in particular might be sequestration in a less volatile form, in which case the observed mixing ratios would not reflect the total molecular abundance in the comet. This possibility is discussed further in Section 8.1.

4.2. CH_4

Methane ice forms in the molecular cloud by hydrogenation of carbon atoms and ions adsorbed onto the grains, and its abundance does not change appreciably with time or with radius over much of the disk. Only around its snowline can the observed cometary mixing ratios be matched.

4.3. C_2H_2 and C_2H_6

Both C_2H_2 and C_2H_6 have low abundances in the molecular cloud, where $\text{C}_2\text{H}_2/\text{H}_2\text{O} = 0.02\%$ and the C_2H_6 ratio is a factor of 11 lower. The comet abundances range from 0.04 to 0.4% for $\text{C}_2\text{H}_2/\text{H}_2\text{O}$, and from 0.26 to 2% for C_2H_6 . Therefore to fit the observations, these two molecules must form in the disk.

The models fit the observations of C_2H_2 between a range of times and locations after 0.1 Myr and inside of 18 au. Formation at early times (< 0.1 Myr) is by freezeout of gas-phase hydrocarbon ions and neutrals (C_2H_3^+ , C_2H_5^+ , C_3H_7^+ , and C_2H_2). Cosmic-ray photon destruction of C_2H_6 ice also plays a role. Hydrogenation of C_2H is not a major formation route at these times, but does contribute at $t > 0.1$ Myr. Destruction of C_2H_2 is by cosmic-ray photons forming C_2H .

The model predictions for C_2H_6 fit the comet observations either at early times (< 1 Myr) inside of 15–20 au, or after 1 Myr at $R > 20$ au. The formation process depends on the time and location, with freezeout of gas-phase ions (mainly C_3H_7^+) dominating at smaller radii and sequential hydrogenation of C_2H at larger radii.

4.4. HCN

$\text{HCN}/\text{H}_2\text{O}$ is fairly constant over the disk with time and radius. Its initial abundance is 3.2%, higher than observed in comets (0.07%–0.5%), and the comet data is only fit in regions where desorption is efficient (i.e., near this molecule’s snowline, around 6–7 au). At larger radii, it is formed by freezeout of HCN or HCNH^+ , or by reaction of CN and H on the grains. It is destroyed by cosmic-ray photons, reforming CN.

4.5. OCS

The molecular cloud mixing ratio of OCS is very low ($\text{OCS}/\text{H}_2\text{O} = 0.02\%$), and this species mainly forms in the disk from the reaction of CO with sulfur atoms (Equation (4)). Destruction is by cosmic-ray photons forming CS or CO. The disk OCS abundance matches the comets either around its snowline, or outside of 20 au and after 10 Myr.

4.6. NH_3

Ammonia ice forms efficiently in the molecular cloud from hydrogenation of nitrogen atoms in the ice. Its initial abundance is 4.7%. The highest value of $\text{NH}_3/\text{H}_2\text{O}$ observed in a comet is 3.6% in C/2012 S1, an OCC. For the other comets, the ratio is less than half of this. Hence, some loss of NH_3 is required to match the observations. This is achieved in two regions on either side of the CO snowline, at times later than 1 Myr, when NH_3 is destroyed by cosmic-ray photons forming NH_2 and NH . NH_2 is likely to react with H reforming NH_3 , but NH does not do this. Outside of the CO snowline, NH reacts with CO to form HNCO (Equation (3)), whereas at smaller radii, NH can desorb. This results in a loss of NH_3 .

5. Low Cosmic-ray Model Results

Cosmic rays are important drivers of the chemistry in the fiducial model. For the interstellar medium, an ionization rate of $1.3 \times 10^{-17} \text{ s}^{-1}$ is generally assumed, although higher rates have been inferred from observations of H_3^+ in some diffuse regions (McCall et al. 2003; Indriolo et al. 2007). For disks around young stars, Cleeves et al. (2013) suggested that the ionization rate may be lower than interstellar, with a value of

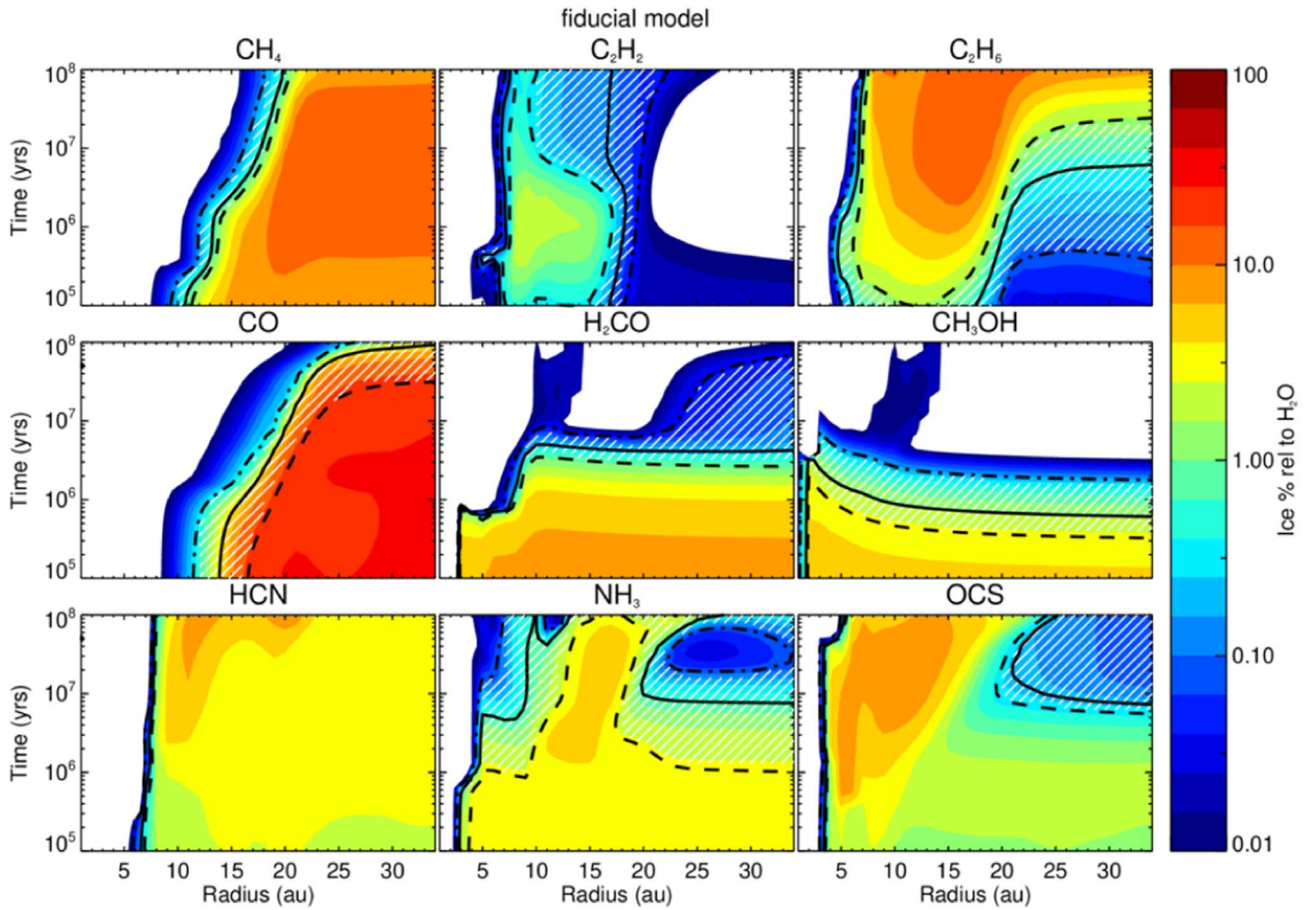


Figure 1. Ice abundances in the fiducial disk model compared with the averages and ranges for the observed comet values in Table 5. Color shading shows the modeled molecular ice abundances relative to H_2O . The white hatched area indicates the range among the observed comets. The upper end of the range is indicated with a black dashed line (---), the lower end by a black dotted-dashed line (- · - · -). The average observed composition is the solid black line. Average observed values are from DR16, except OCS, which comes from Saki et al. (2020).

$0.23\text{--}1.4 \times 10^{-18} \text{ s}^{-1}$. Seifert et al. (2021) showed that the picture may be more complicated, finding a very low value of $\zeta_{\text{CR}} < 10^{-20} \text{ s}^{-1}$ in the inner 100 au of IM Lup, and 10^{-17} s^{-1} outside of this.

To examine what effect a lower cosmic-ray ionization rate might have on the midplane ice abundances, we ran a second model with $\zeta_{\text{CR}} = 1.3 \times 10^{-18} \text{ s}^{-1}$, a factor of 10 lower than the flux in our fiducial model (Figure 3). Longer timescales are required to match the observed range for those species whose chemistry is driven by cosmic-ray processing of the ices. For example, cosmic rays destroy the CO at 5–10 Myr, rather than 0.5–1 Myr as in the fiducial model. The model H_2CO now matches the observations only at $t > 20\text{--}100$ Myr and CH_3OH between 5 and 50 Myr. Unlike the fiducial model, a low cosmic-ray ionization rate cannot fit the entire range of the NH_3 observations at $R > 20$ au, and only the lowest part of the observed OCS range can be accounted for. However, this model is still able to match the observed range of mixing ratios for the other molecules, albeit it at later times than in the fiducial model.

6. “Reset” Model Results

Following other studies of protosolar nebula composition, we also consider a model where any molecular cloud composition is wiped out by the formation of the disk, and the disk chemistry starts with atomic abundances. This could

occur during the infall process, e.g., Visser et al. (2009), or by energetic events in the early solar system. There is evidence for some degree of “reset” in the inner solar system from studies of chondrules and calcium-aluminum-rich inclusions (e.g., Trinquier et al. 2009), but whether this would extend out to the comet formation region is uncertain.

The abundances for the “reset” model are given by Table 3. The resulting disk composition is shown Figure 4. The magnitude and distribution of the mixing ratios are quite different to the fiducial model.

The CO distribution is similar to the fiducial model but much lower. For most of the disk, the ratio of $\text{CO}/\text{H}_2\text{O} \sim 1\%$. It does reach $\sim 5\%$ at times earlier than 0.1 Myr, but this is much lower than the ratio seen in many comets. CO ice is converted into CO_2 , HNCO , and OCS. H_2CO and CH_3OH , molecules that are derived from the hydrogenation of CO, are both underabundant compared to the fiducial model. While H atoms are abundant at the start of the disk model, there is an activation barrier to hydrogenation of CO. The warmer temperatures in the disk compared to the molecular cloud model help to overcome this. They also mean that the residence time of H atoms on the grains is reduced and that other reactions of CO (with NH and S) are also faster than in the molecular cloud, and hence the formation of H_2CO and CH_3OH is less efficient. The “reset” model can account for the lowest mixing ratios of these

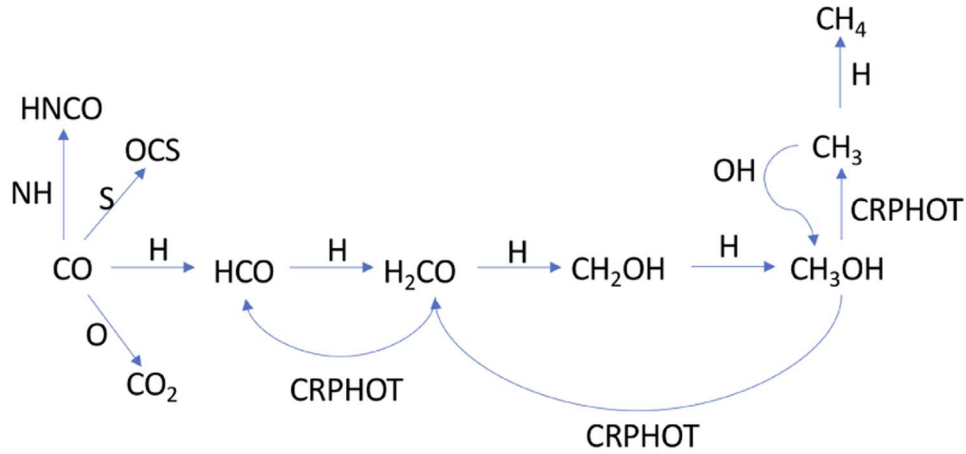


Figure 2. The grain chemistry of CO, H₂CO, and CH₃OH. All species shown are ice molecules. H₂CO and CH₃OH must be reduced from their molecular cloud abundances to fit the comet observations; this is achieved by processing of the ice by cosmic-ray photons.

molecules in comets, but it cannot account for the full range of observations.

C₂H₆ matches the observations on either side of the CO snowline. This distribution resembles that seen in Figure 1, but the match to observations occurs at earlier times. C₂H₂ on the other hand is much more abundant than in the fiducial model with ratios of >10% at 8–10 au. The fiducial model matches the observations of C₂H₂ around the CO snowline, but in the “reset” model, the match is either at $R > 15$ au, or at 6–10 au, depending on the time.

The “reset” model can at least partially match the HCN observations at larger radii ($R > 15$ au) than was possible in the fiducial model. The NH₃ observations are matched either at late times ($t > 1$ Myr) and outside of 20 au, or at smaller radii at all times. The model OCS only agrees with the observed range around its snowline.

Overall, the “reset” model is unable to account for the complete range of observed abundance ratios.

7. Comparison of Observations in JFCs and OCCs

The results above show that the fiducial model can account for the complete range of abundances in Table 5, as reported in DR16 and Saki et al. (2020). We now consider whether there are any systematic differences between the JFCs and OCCs. One caveat to this discussion is that the observed abundance ranges we use are based on a relatively small number of measurements and so are unlikely to represent the complete range of possible abundance ratios in comets. In particular, the number of measurements in JFCs is quite small. Therefore any conclusions regarding the differences between the families are tentative because they could be a result of the small sample size. Comparing the models to the observed ranges suggests the differences between the JFCs and OCCs are small (Figure 5). The molecule with the biggest difference is CO, whose abundances span a greater range in OCCs than JFCs, corresponding to a larger range of radii in the model protosolar nebula. This difference is enhanced if the observed upper limit is taken to be the largest individual measurement in Hale-Bopp (41%) rather than the weighted average of 26% in this comet. With this higher value, the outer radius of models that fit the OCC range is now 35 au rather than 18 au at 0.1 Myr. NH₃ also shows some differences between the two families, with a larger range of model times required to fit the OCC observed range. A

similar effect is seen for H₂CO and C₂H₆. For other molecules though, the combinations of location and time that fit the observed range show little difference between the two families.

A’Hearn et al. (2012) used observations of CO, CO₂, and H₂O to investigate where JFCs and OCCs formed. They found that JFCs and OCCs formed in overlapping regions, with JFCs on average slightly closer to the Sun. This is consistent with our results if the highest CO/H₂O ratio observed in Hale-Bopp is taken into account. In particular, the narrower range of CO mixing ratios in JFCs is fit by the model disk’s ices only around the CO snowline, whereas for OCCs, the larger range of CO mixing ratios could allow some to form as far out as 35 au. However, this is the opposite of the classical picture where JFCs form beyond Neptune and OCCs in the region of the giant planets before being scattered to their current reservoirs (Rickman 2010).

Alternatively, JFC abundances may reflect their time spent as Centaurs orbiting among the outer planets. Here, the outer kilometer or so of the nucleus can be heated by sunlight to 80 or 90 K (Guilbert-Lepoutre et al. 2016), sufficient for some of the more-volatile species to be partially lost (Lauck et al. 2015). Such losses may account for the JFCs’ generally lower CO abundances, if today’s JFCs retain some of the thermally processed material. However, it is unclear whether there is a thermally processed layer, and if so how much of the present-day outgassing comes from this material rather than the less-processed interior of the nucleus. Enough perihelion passes near the Earth’s orbit would remove the thermally processed layer, revealing the bulk nucleus. This appears to be the case for 67P, where the presence of N₂ suggests that any thermally processed material has already been lost (Rubin et al. 2015).

8. How Did Comets Obtain Their Compositions?

8.1. Assembly from Material at a Single Time and Location

While the previous section has shown that the fiducial and low cosmic-ray models can match the observed range of each molecule *individually*, the question now is whether they can provide an explanation of the complete composition of each comet as a whole. To determine how well our models account for the *overall* comet compositions, we compare them to a subset of individual comets from our sample, consisting of the JFCs 103P/Hartley 2 and 9P/Tempel 1, and the OCCs C/1999 H1 (Lee), C/2009 P1 (Garradd), C/2013 R1 (Lovejoy),

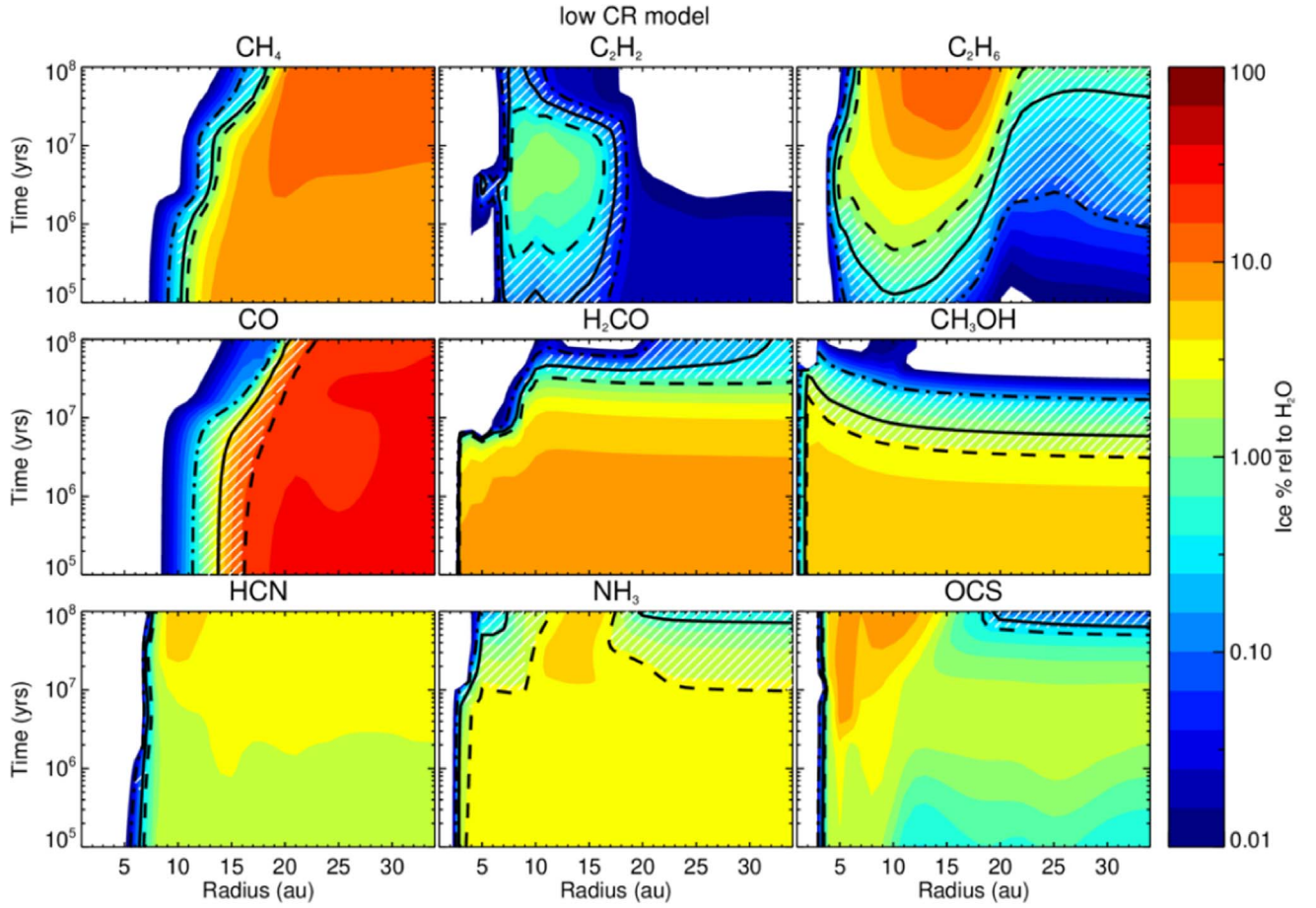


Figure 3. Calculated abundances (filled colored contours) from the model with low cosmic-ray flux compared to the observed abundance ranges in all comets in Appendix B.

C/2007 N1 (Lulin), C/2012 S1 (ISON), and C/2004 Q2 (Machholz). Each of these comets has observations for all eight molecules discussed in DR16, although only upper limits are available for CH_4 in Hartley 2 and for H_2CO and C_2H_2 in Lovejoy. For ISON, we use the data listed in Table 2 of DR16 as coming from ≥ 0.83 au since this has the most complete set of molecules. Where upper limits only are available, we assume the mixing ratio to be half of the upper limit. In addition, OCS observations are available for comets Lovejoy, Garradd, ISON, and Lee (Saki et al. 2020). For this analysis, we use the fiducial model, since the “reset” model cannot match the complete range of observed mixing ratios.

In addition to the individual comets, we also analyze the average composition for JFCs and OCCs from Table 5. Although no comet has this exact composition, the averages do serve as a means of determining if there are any systematic differences in the times and locations at which the different families might have formed.

To assess whether the models provide a good fit to the data, we use the χ^2 test. For each combination of location and time for our fiducial model, we calculate the value of χ^2 from

$$\chi^2 = \sum_{i=1}^n \frac{(O_i - M_i(r, t))^2}{M_i(r, t)} \quad (7)$$

where O_i is the observed mixing ratio relative to water ice of molecule i , and $M_i(r, t)$ is the mixing ratio i relative to water ice for a model at radius, r , and time, t . A good fit of the models to

the observations at a 95% confidence level requires $\chi^2 < 14.07$ for comets without OCS observations and $\chi^2 < 15.5$ for those with measured OCS. Note that Eistrup et al. (2019, hereafter E19) carried out a similar analysis but used a slightly different version of χ^2 since they were comparing the logarithm of the observations and models. Use of their formulation results in some differences in the calculated χ^2 values but does not change our overall conclusions.

The calculated χ^2 values obtained by comparing the observations with the fiducial model are shown in Figure 6. The lowest values of χ^2 are found around the CO snowline, in agreement with the results of E19. The location and time for the best fit for each comet are listed in Table 7. However, in each case, the lowest calculated χ^2 is above the limit required for a good fit at the 95% confidence level.

The lowest χ^2 values found for the average JFC and OCC compositions are in similar locations, with a radius of 13 au for JFCs and 14 au for OCCs. For the individual comets, the locations range from 10 au (for Comet Hartley 2) to 15 au for Lovejoy and Garradd, and the times from 0.08 Myr (Comet Hartley 2) to 0.5 Myr (for comets Tempel 1 and ISON). It is perhaps not surprising that the χ^2 suggests that the models at a single location and time are not a good fit to the overall composition of the comets, as Figure 1 shows that the molecules come from different (non-overlapping) regions in the disk. For example, the predicted HCN mixing ratios only cover the observational range close to its iceline around 6 au,

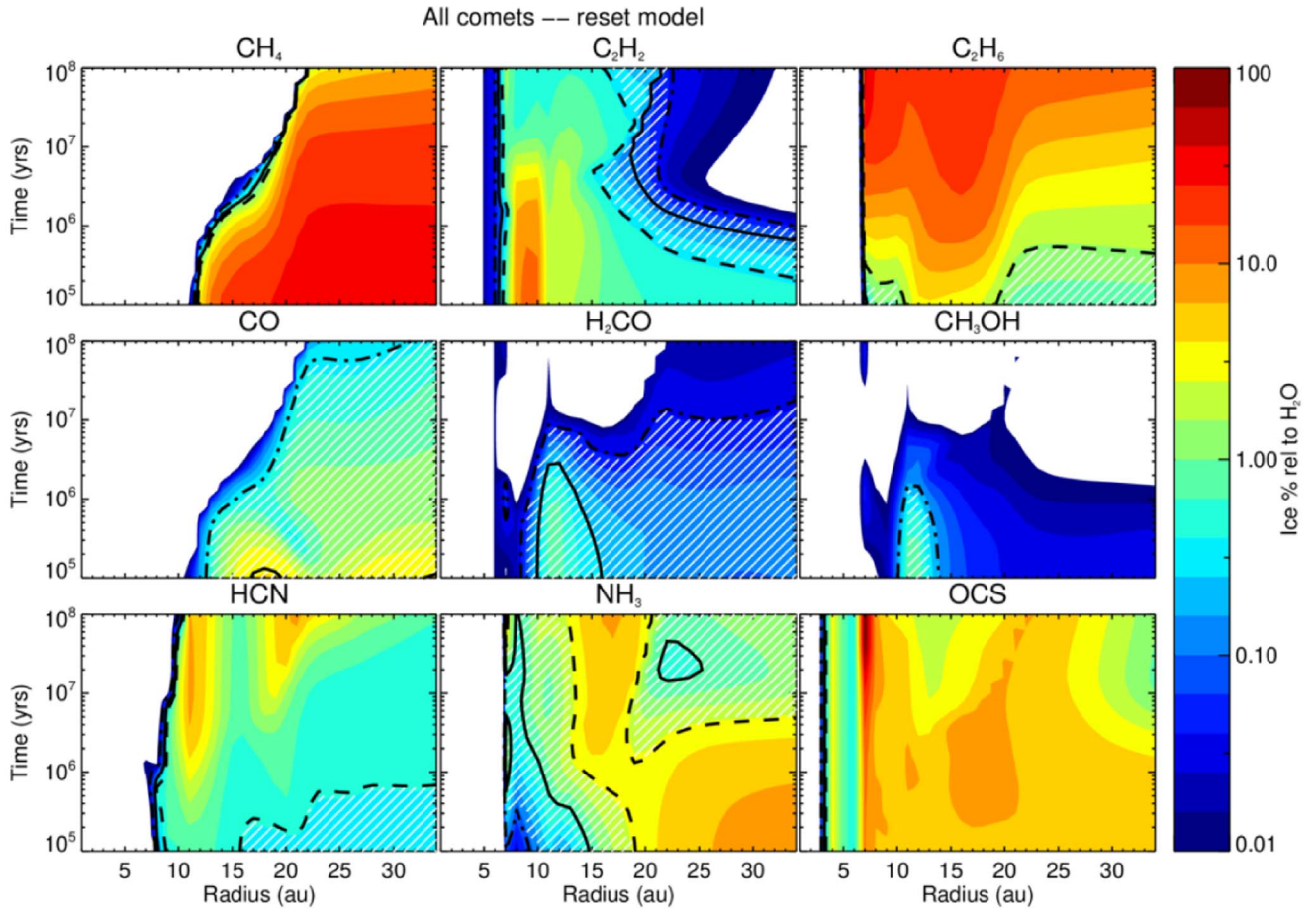


Figure 4. Predicted molecular distributions for the “reset” abundance inputs (colored contours). Markings are the same as in Figure 1.

Table 7
Best-fit Models from a Single Radius and Time to the Observational Data

Comet	χ^2	R (au)	Time (Myr)	Molecules Not Fit by Lowest χ^2 Model
9P/Tempel 1	23.2	14	0.50	HCN, NH ₃ , H ₂ CO, C ₂ H ₆
103P/Hartley 2	19.9	10	0.08	HCN, H ₂ CO
C/1999 H1 Lee	20.3	13	0.32	HCN, H ₂ CO
C/2004 Q2 Machholz	24.3	14	0.04	HCN, NH ₃ , H ₂ CO, CH ₄ , C ₂ H ₂ , C ₂ H ₆
C/2007 N1 Lulin	21.1	13	0.25	HCN, NH ₃ , H ₂ CO, C ₂ H ₂
C/2012 S1 ISON	20.1	13	0.50	HCN, C ₂ H ₆
C/2009 P1 Garradd	28.1	15	0.40	HCN, H ₂ CO, C ₂ H ₂
C/2013 R1 Lovejoy	30.3	15	0.25	HCN, NH ₃ , H ₂ CO, C ₂ H ₆
Average OCC	24.9	14	0.32	HCN, H ₂ CO
Average JFC	25.1	13	0.40	HCN, H ₂ CO, C ₂ H ₂ , C ₂ H ₆

Note. Molecules listed are those that cannot be fit by these models to within a factor of 10 of the observed value. Good fits are provided by models with $\chi^2 < 14.07$ for comets with eight observations (9P/Tempel 1, 103P/Hartley 2, C/1999 H1 (Lee), C/2004 Q2 (Machholz), and C/2007 N1 (Lulin)), and < 15.5 for those with nine observations (C/2009 P1 (Garradd), C/2012 S1 (ISON), and C/2013 R1 (Lovejoy)).

much closer to the star than the location of the lowest χ^2 models.

In the literature, good agreement between individual observations and astrochemical models is often taken to be a factor of 10. This allows for errors in the observational data, as well as in the models themselves. The final column in Table 7 lists the molecules for which the predicted abundances of the best-fit model deviate from the observations by more than this. None of the models can fit HCN, and in several comets, H₂CO,

C₂H₂, and C₂H₆ are not matched either. For the average compositions, the models cannot fit HCN and H₂CO, with C₂H₂ and C₂H₆ also in poor agreement with the average JFC values.

Using Hartley 2 as an example, we look at the size of the discrepancy between observations and models at the location of the lowest χ^2 . The observed mixing ratio for HCN is 0.24%, but at $R = 10$ au and $t = 0.08$ Myr, the model predicts HCN/H₂O = 3.2%, a difference of a factor of 13. The

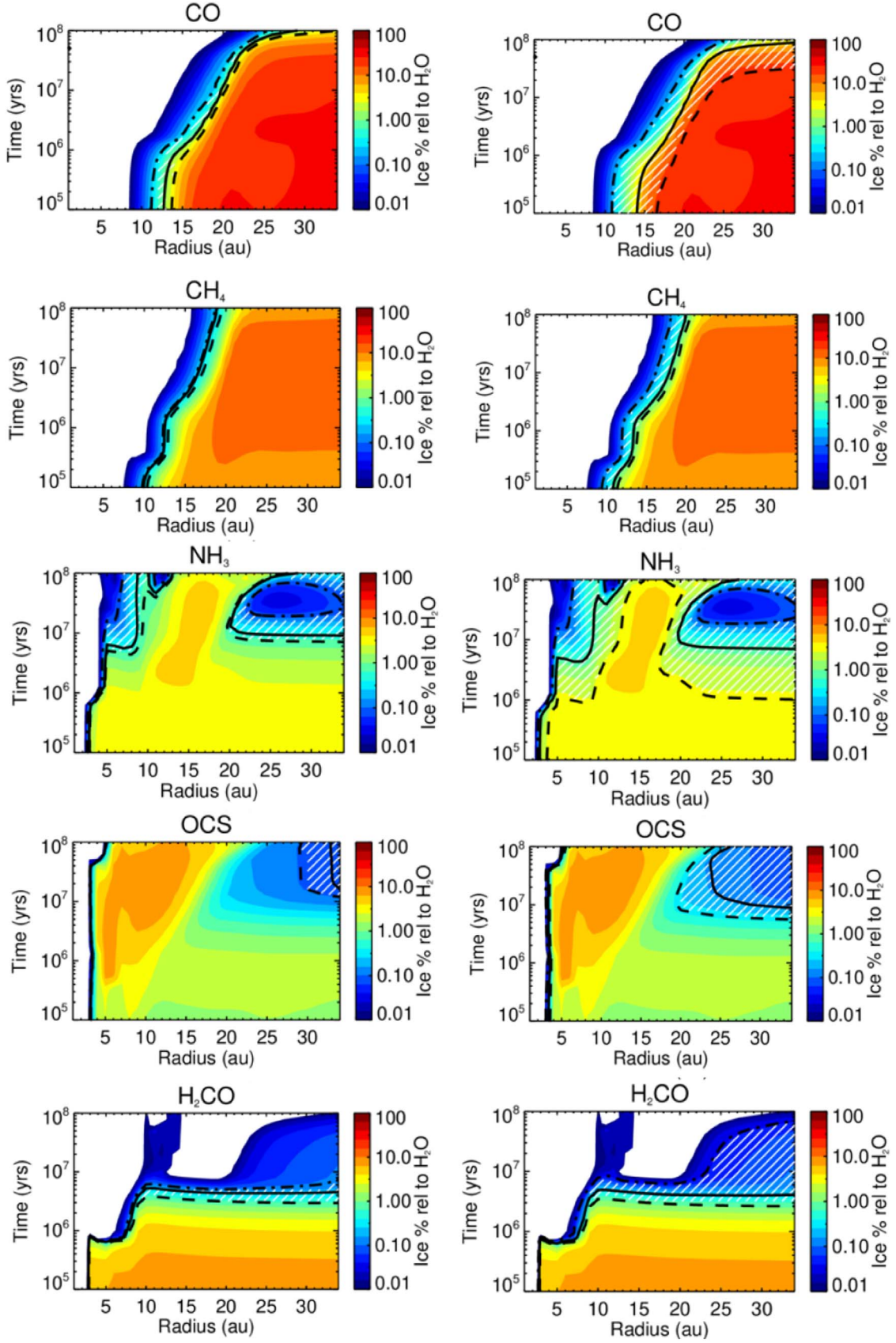


Figure 5. Average and range of the JFC (left) and OCC (right) family observations, showing the range of disk times and locations that fit the observed mixing ratios relative to H₂O from Table 5. Lines and symbols are the same as in Figure 1 for each comet family.

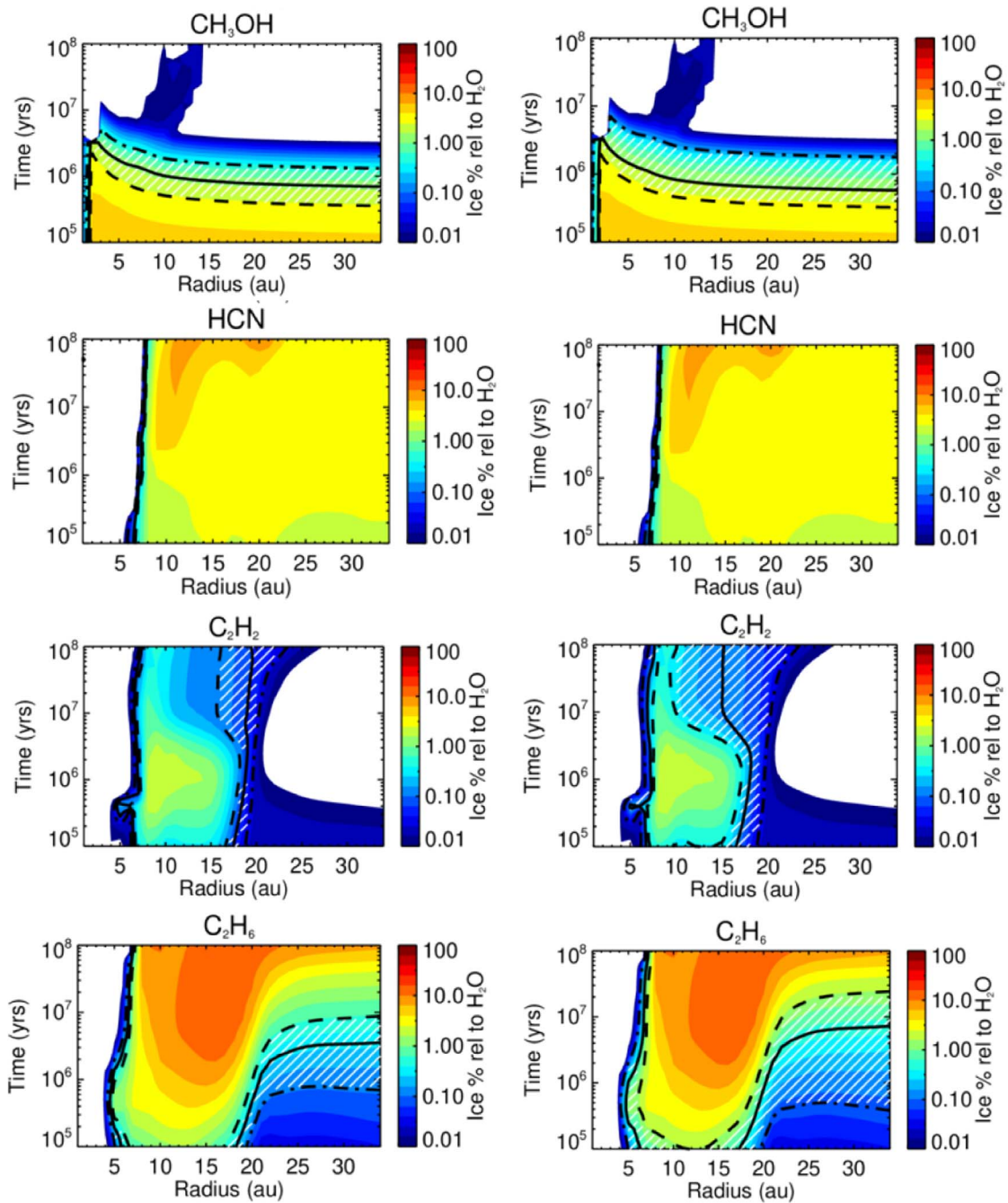


Figure 5. (Continued.)

difference in the observed and predicted mixing ratios of H_2CO at this location is even higher—a factor of 64. The predicted abundances from a single location and time in the protosolar nebula therefore do not provide a good match to the overall composition of our comets. We now investigate a mechanism to improve the agreement.

8.2. Disk Mixing: Combining Material from Two Locations

The distribution of molecules seen in Figure 1 suggests that combining material from different radii might result in a closer match to the observed comet compositions. Disks experience widespread turbulence, likely resulting in radial and vertical mixing throughout. Both mechanisms would bring material

processed in warmer and/or higher UV regions, where more-volatile species such as CO have been lost, into regions with CO-rich ices where they could combine to form protocomets. We explore this possibility with a toy model that combines material from inside and outside the CO iceline. Although not a physically complete solution, this model explores a potential means of explaining the range of thermal histories required to explain material incorporated into cometary nuclei. We note that this is not “the solution,” and a more complex exploration of parameters, such as 2D (vertical and radial) mixing, is likely needed and will be the focus of future work.

There is observational evidence for the idea that inner disk material was incorporated into comets. The presence of

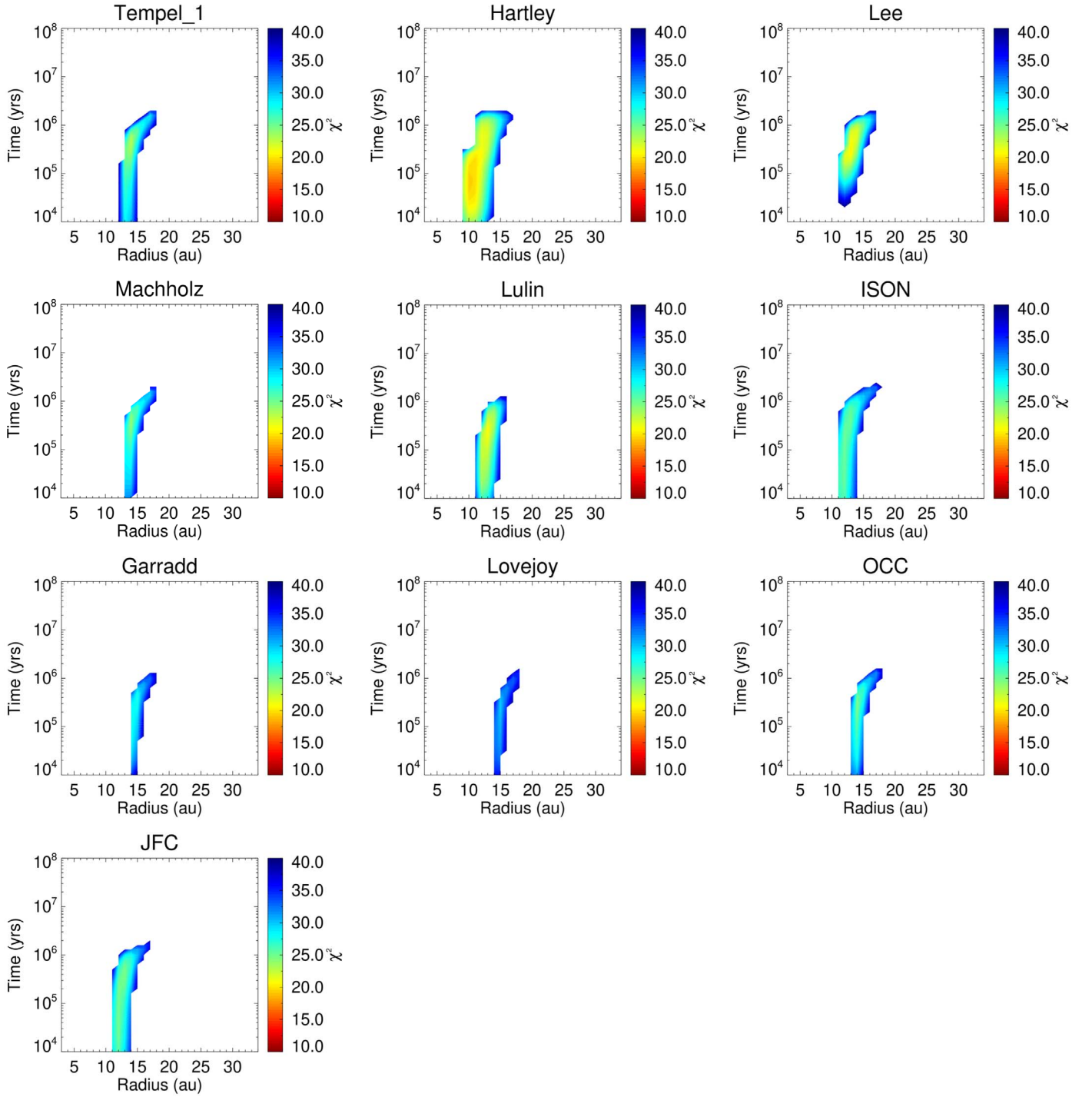


Figure 6. Plots of χ^2 calculated by Equation (7) comparing observations of individual comets with models.

crystalline silicates in some comets (Bregman et al. 1987; Crovisier et al. 1996; Zolensky et al. 2006) indicates that they include material processed at high temperatures from close to the star into their nuclei. Note that temperatures high enough to form crystalline silicates are not required for the scenario we are exploring here.

We consider a scenario where grains from two radii, R_1 and R_2 , are combined. Since comets contain CO and N₂, we assume that they must form outside of the CO snowline, and that grains from inside the snowline are transported outward to this

location. To achieve the observed composition, we therefore assume that material is transported from the inner disk (where the models can fit HCN) to the outer disk without any changes to its composition. We contend that this is a reasonable assumption since (a) mixing from warm to cold regions will not induce any desorption, and (b) condensation of new material is unlikely since any species that can be condensed at R_2 will already have done so on grains that are already present. The inner disk ice composition is therefore likely to be preserved as it travels outward to the comet formation zone. The travel time

from R_1 to R_2 may allow for chemistry to alter the composition, or for gas traveling with the grains to condense, but the complex modeling to simulate these effects is beyond the scope of this manuscript. More sophisticated models incorporating coupled transport and chemistry are required to clarify whether these mechanisms play a role in determining ice compositions and will be addressed in future works.

The fiducial models discussed in Section 4 provide molecular abundance relative to H_2O as a function of time and radius in the disk. We use these results to determine whether material from two different locations can be combined to provide better agreement with the observations than those from a single time and radius. For each model time step between 10^4 and 10^8 yr, we combine the abundance predictions from two radii, R_1 and R_2 , in different proportions and determine whether the models can fit the data. We assume that the two radii come from inside (R_1) and outside (R_2) the CO snowline. R_1 is chosen from 3–10 au, and R_2 from 10–25 au, in increments of 1 au. We take each value of R_1 in turn and combine it with each possible value of R_2 , with proportions of R_1 from 0.05–0.95 (in steps of 0.05) of the total comet composition. The combined ice composition is then given by

$$\text{combined composition} = f_{R_1} \frac{n_{R_1}(X)}{n_{R_1}(\text{H}_2\text{O})} + (1 - f_{R_1}) \frac{n_{R_2}(X)}{n_{R_2}(\text{H}_2\text{O})} \quad (8)$$

where f_{R_1} is the fraction of the total comet composition from R_1 , and $n_{R_1}(X)$ and $n_{R_2}(X)$ are the ice abundances of X at R_1 and R_2 , respectively. In this way we can make a grid of compositions that cover all possible combinations of R_1 and R_2 , resulting in a total of 104,386 combined compositions. We compare each with the comet observations and calculate the χ^2 . To check that the models are able to produce a reasonable agreement with each molecule’s observed values, we also determine whether all eight (or nine if OCS is observed) of the measured mixing ratios match the model predictions to within a factor of 10. A good fit is therefore defined by (a) $\chi^2 < 14.07$ (15.5) for eight (nine) observed molecules (criterion C1), and (b) the models matching the observations to within an order of magnitude (criterion C2).

We find that for all comets considered here that there are a range of models with different combinations of R_1 , R_2 , and f_{R_1} that fit both criteria. Table 8 lists the parameters of the combination of models with the lowest χ^2 value. All comets require a large contribution of material from inside of the CO iceline.

Figure 7 shows the best-fit models to the average comet data. The figure shows the contour plots of χ^2 overlaid by symbols indicating the models for which all of the observed molecules are matched to within a factor of 10. For the average composition of both the OCCs and JFCs, the lowest χ^2 is achieved by combining models from 3 au and 18 au, but the contribution from the two radii is different for the two families, with JFCs requiring 90% from 3 au compared to 80% for OCCs. There is a range of contributions from R_1 and R_2 that satisfy both criteria for good fits (i.e., $\chi^2 < 15.5$ and all abundances within an order of magnitude of the observations). These models are indicated on the plot by the blue diamonds. Models fit the data for the average OCC composition for both

Table 8
Best-fit Parameters Assuming Comets Are Made from Material from Two Radii in the Fiducial Model, One Inside (R_1) and One Outside (R_2) the Snowline

Comet	Time	R_1 (%)	R_2 (%)	χ^2
9P/Tempel 1	1.0 Myr	4 (85%)	18 (15%)	3.9
103P/Hartley 2	2.0 Myr	4 (90%)	17 (10%)	0.9
C/1999 N1Lee	1.3 Myr	4 (85%)	17 (15%)	1.8
C/2004 Q2 Machholz	1.6 Myr	4 (85%)	19 (15%)	2.8
C/2007 N1 Lulin	1.0 Myr	3 (90%)	18 (10%)	0.9
C/2012 S1 ISON	0.5 Myr	3 (85%)	15 (15%)	9.4
C/2009 P1 Garradd	1.6 Myr	3 (75%)	19 (25%)	6.8
C/2013 R1 Lovejoy	2.5 Myr	3 (80%)	20 (20%)	12.3
Average OCC	1.0 Myr	3 (80%)	18 (20%)	4.8
Average JFC	1.6 Myr	3 (90%)	18 (10%)	2.0

Note. Shown are the combinations of R_1 and R_2 with the lowest χ^2 that also match the observed abundances of each molecule to within a factor of 10. The contribution of each radius is given as a percentage of the total calculated composition (so percentage of R_1 given is $100 \times f_{R_1}$, where f_{R_1} is the fraction of R_1 in Equation (8)). The composition of our entire comet sample can be matched by such combined models. Good fits are provided by models with $\chi^2 < 14.07$ for comets with eight observations (9P/Tempel 1, 103P/Hartley 2, C/1999 H1 (Lee), C/2004 Q2 (Machholz), and C/2007 N1 (Lulin)), and < 15.5 for those with nine observations (C/2009 P1 (Garradd), C/2012 S1 (ISON), and C/2013 R1 (Lovejoy)).

criteria with a contribution from 40%–90% from 3 au at times between 0.7 and 1.2 Myr. JFCs require a contribution of between 70% and 95% from 3 au at times from 0.8 to 3 Myr. This would suggest that the JFCs formed from warmer material than the OCCs. It should be noted that there are other values of R_1 and R_2 that are also able to match the observations.

The same information for the individual comets is shown in Figure 8. One combination of radii is shown (the one for which χ^2 is lowest), but there is a range of different combinations of R_1 and R_2 that have χ^2 below the value required for a good fit and where the model abundances are within a factor of 10 of the observations. All of the comet compositions can be matched by combinations of models from two radii. It should be noted that while for most of the comets the model with the lowest χ^2 also predicts abundances that are all within a factor of 10 of the observations, this is not the case for Lovejoy. For this comet, the models that satisfy both fitting criteria have a slightly larger value of χ^2 than the minimum. The models here are not sufficient to pin down the exact formation location and history of comets but do illustrate that more than one component is required to fit the observations.

9. Discussion

We have constructed a model of the chemistry of the protosolar nebula and investigated whether this can account for the current observed average, minimum, and maximum abundances of nine molecules in comets: CO, CH_4 , H_2CO , CH_3OH , C_2H_2 , C_2H_6 , NH_3 , HCN, and OCS. Two of our models—the fiducial (with $\zeta_{\text{CR}} = 1.3 \times 10^{-17} \text{ s}^{-1}$) and low cosmic ray ($\zeta_{\text{CR}} = 1.3 \times 10^{-17} \text{ s}^{-1}$)—are successful in reproducing the current observed range of mixing ratios in comets. The ices of six of the molecules we consider (CO, CH_4 , NH_3 , H_2CO , CH_3OH , and HCN) appear to be inherited from the parent molecular cloud and either reflect the molecular cloud abundances with little change (CO), or require partial

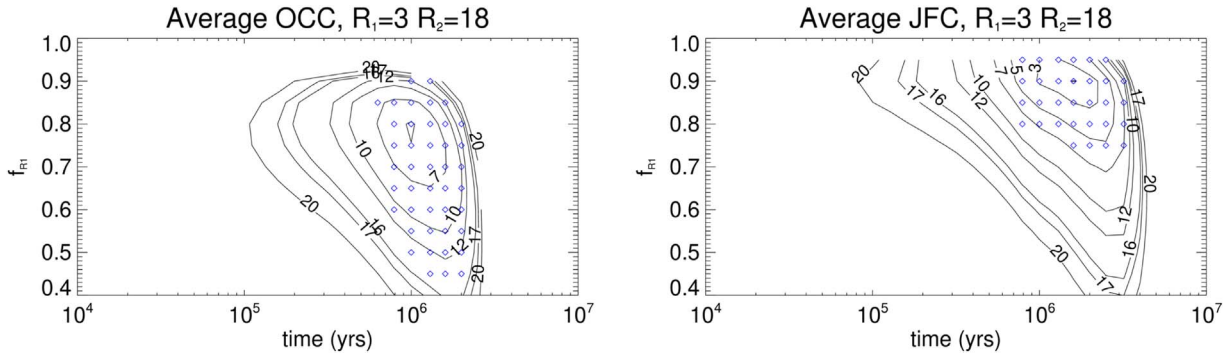


Figure 7. The best-fit models using combinations of two radii (one from inside the CO snowline (R_1), and one from outside it (R_2) to the average comet compositions. χ^2 was calculated for all models for all combinations of R_1 from 3–10 au and R_2 from 10–25 au. f_{R1} is the fraction of material from R_1 , with the values of R_1 and R_2 given in the plot title. The contribution of R_1 to the total composition was varied from 5%–95%. Shown here are the calculated χ^2 for the best-fit R_1 and R_2 over all times and contributions. The symbols show where all observed molecules are matched by the models to within a factor of 10.

reprocessing during infall, or in the disk by thermal desorption, cosmic rays, or grain surface reactions (HCN, NH_3 , CH_4 , H_2CO , and CH_3OH). Although the observed range of each molecule can be matched by the fiducial and low cosmic-ray models, no single time and location in any of our models can match all nine of the molecules simultaneously.

CO is not produced in our fiducial disk model; hence, the highest abundance predicted is set in the molecular cloud model. However, since CO is extremely volatile, it is likely that its abundance was affected by desorption during the disk formation process and would therefore be lower than its molecular cloud value. This would create a problem for the models to be able to account for the more CO-rich comets. It is possible that some of the observed CO comes from the destruction of more complex molecules (Disanti et al. 1999), meaning that the observed abundance will be higher than that contained in the ices of the comet nucleus.

Cosmic rays play an important role in determining the abundance distributions of NH_3 , H_2CO , and CH_3OH . The flux of cosmic rays in disks is still uncertain, and there is evidence from current PPDs that the flux could be reduced (perhaps significantly) in the inner 100 au (Seifert et al. 2021; Cleeves et al. 2013). While reducing the cosmic-ray flux by a factor of ~ 10 still allows our models to account for the full range of observations but at later times than the fiducial model, reducing ζ_{CR} still further results in little change in the ice abundances compared to the molecular cloud. A model with such low cosmic-ray flux would require photoprocessing of ices. This could be achieved by mixing within the disk, either vertical or radial.

Other molecules, such as HCN and CH_4 , agree best with the cometary data near their snowlines, where their abundances are reduced compared to their initial values, and hence brought closer to the cometary values. Another way to bring their abundances into agreement with observations would be if they were formed less efficiently in the molecular cloud. Both molecules form by hydrogenation on the grain surfaces: HCN from CN, and CH_4 from carbon atoms. Reducing their abundance in the molecular cloud model could extend the range of radii over which the disk models can match the observations. CH_4 , like CO, is also very volatile, and therefore some methane ice may be expected to be lost during the star/disk formation.

C_2H_2 and C_2H_6 differ from the molecules above in that their predicted molecular cloud values are lower than in the comets, requiring formation in the disk, either by freezeout of gaseous

hydrocarbons or their ions, or by hydrogenation of unsaturated hydrocarbons in the ices.

Our “reset” model, which assumes any molecular cloud chemistry is wiped out during the disk formation, is less successful and cannot account for the full range of observed abundances. In particular, the CO abundance, while showing a similar distribution to the fiducial model, is considerably lower. This also leads to lower CH_3OH and H_2CO abundances. Because the grains are warmer in the disk compared to the molecular cloud, the formation of these two molecules is not as efficient since the lifetime of H atoms on grains is shorter. Instead, CO is processed into CO_2 , HNC, and OCS.

To quantify the ability of the models to account for the observations, we use the χ^2 test. Based on this, the single location and time in the model where the ices best match the cometary observations is near the CO snowline. However, the values of χ^2 are too high to be classed as a good fit, and in addition, the abundances of several species differ by more than an order of magnitude between the model disk and the comets. Other locations in the model disk better fit some of these discrepant ices. For example, HCN only matches the observations well inside the CO snowline. Ammonia on the other hand, has a peak in abundance near the CO snowline, and the best match to the observations is away from this location. Because no single location and time is a good match for the compositions of the tested individual comets, it seems plausible that these bodies incorporate materials formed at different distances from the young Sun.

Since the single location/time models are not able to account for the overall comet compositions, we consider an alternative scenario. Comets comprise a large number of molecules with very different desorption temperatures, and although the molecules are also present in the interstellar medium, their abundances are different, indicating processing is required in the disk. The predicted abundance of HCN in the molecular cloud model is considerably above the range of values seen in comets, and therefore some loss of this species needs to occur in the disk. This only happens in regions where the temperature is too high to allow more-volatile species such as CO to remain on the grains, suggesting that comets are made up of some combination of material that has remained at cold temperatures and thus retains its interstellar composition, together with other grains that have lost at least some of their volatiles through processing at warmer temperatures. Combinations of this kind could arise due to the transport of gas or solid bodies within the

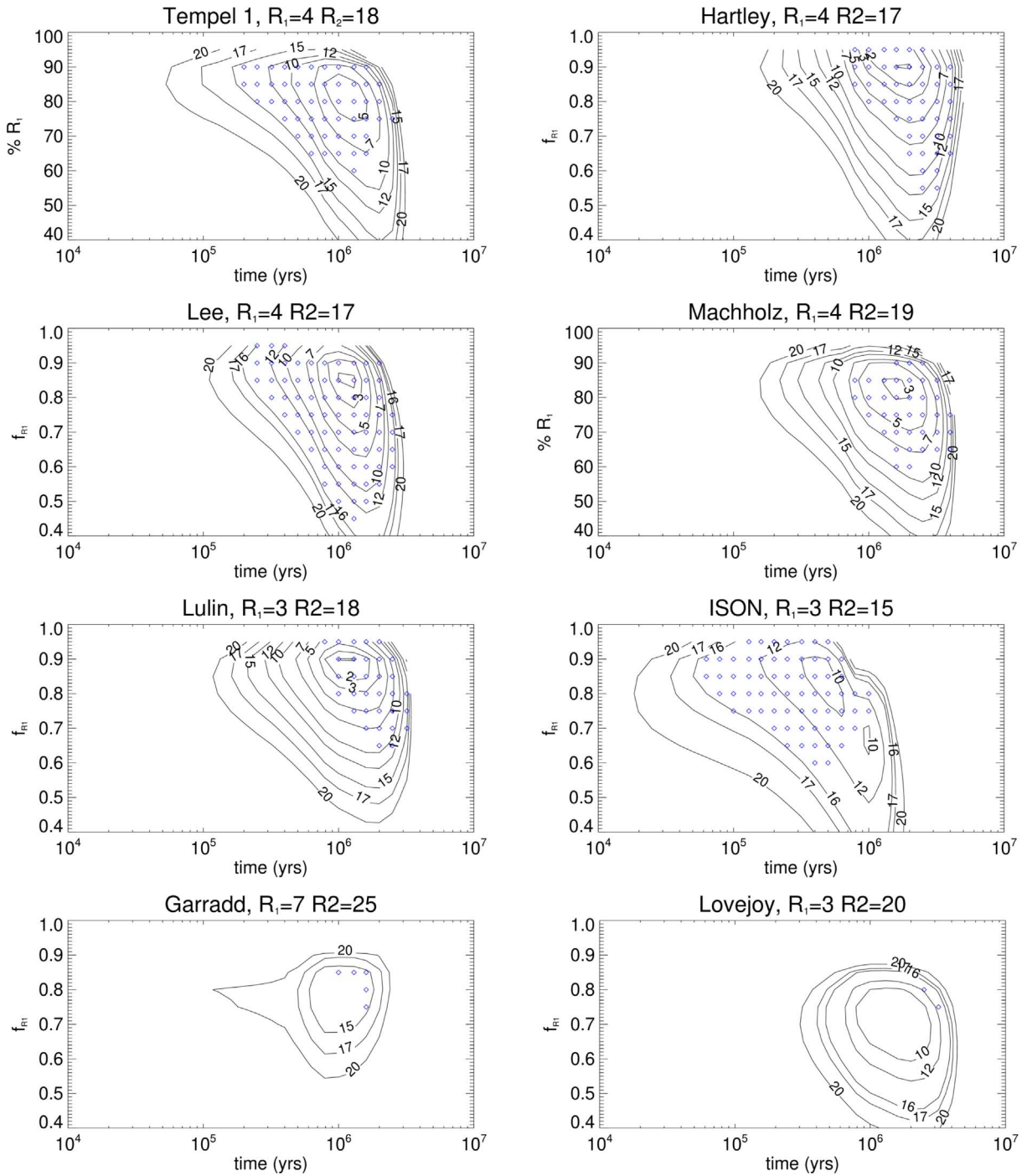


Figure 8. The best-fit models using combinations of two radii (one from inside the CO snowline (R_1), and one from outside it (R_2)) to individual comets. f_{R1} is the fraction of material from R_1 , with the values of R_1 and R_2 given in the plot title. Contours show the χ^2 values, while the blue diamonds indicate models where predicted mixing ratios of all molecules are within a factor of 10 of the observed values.

disk between locations providing distinct temperatures, pressure, and radiation environments.

To explore how the observed comet compositions could have been achieved, we constructed a toy model that combines material from inside and outside the CO snowline. This dividing line was chosen because of the need to retain very volatile ices in our model comet. We find that combining material from these two regions can indeed provide a better agreement with comet observations for all of our sample, as

well as the average comet compositions for both JFCs and OCCs. There is a wide range of model radii and times that can be combined to match the observations. More detailed modeling is required to constrain how particular comets obtained their particular compositions.

There is no obvious difference between the combination of material required for the individual comets comprising two JFCs and the seven OCCs. For the two-radii model, the contributions to the JFCs and OCCs come from overlapping

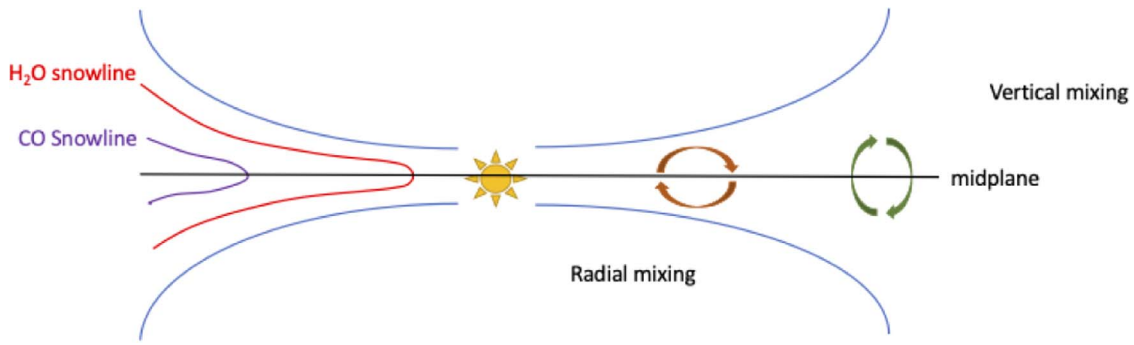


Figure 9. The location where CO desorbs depends on both the radial and vertical location. While in the midplane there is a clear snowline at the radius at which the desorption temperature of CO is reached, there is also one above the midplane where the gas and dust closer to the disk surface is heated sufficiently. This means that CO-depleted ice can have its origin either at small radii in the midplane, or above the midplane at larger radii. Consequently, mixing from either direction (or both) could be the source of the CO-poor material suggested by our modeling

regions. This is consistent with the conclusions of A’Hearn et al. (2012) based on observations of the three molecules CO, CO₂, and H₂O, but is in conflict with the classical picture of comet formation in which JFCs were formed outside of Neptune’s orbit and OCCs closer to the star. However, the number of comets observed in each family is small, especially for JFCs, and therefore it is difficult to draw definitive conclusions about the differences between the two families based on the current observations. However, from the average compositions, it does appear that the JFCs require a higher fraction of their composition to be CO-poor. Further understanding of the links between comets and the protosolar nebula will require remote observations of more comets, models treating the disk’s chemistry alongside its gas dynamics and grain growth and transport, and ultimately, close-up visits by spacecraft to cometary nuclei with a range of dynamical histories.

9.1. Transport in Disks

The mix of CO-rich and CO-poor material required for the disk models to match the comet observations suggests efficient transport in the protosolar nebula. The exact nature and efficiency of such mixing is beyond the scope of this paper, but here we briefly discuss some of the main points.

Evidence for transport in the protosolar nebula comes from the presence of crystalline silicates in comets (e.g., Brownlee et al. 2009). Cosmic rays destroy silicates’ crystalline structure in the interstellar medium (Kemper et al. 2004), so the comets’ crystalline silicates cannot be interstellar in origin and must have been heated to temperatures near 1000 K found in our young solar system only close to the Sun. How enough crystalline material was carried out beyond the CO snowline is unclear. Radial transport of crystalline silicates appears to occur in contemporary protostellar disks (van Boekel et al. 2004).

The motions of solids in a disk depends on their size. Small grains can be transported with the gas, and outward motion can be achieved by advection or by turbulent diffusion (see reviews by Testi et al. 2014; Turner et al. 2014). Mixing icy grains has previously been suggested as a means of accounting for the D/H ratio observed in comets (e.g., Mousis et al. 2000; Yang et al. 2013). Turbulence leads to small particles making random walks through the disk, giving each its own thermal history. Pebble-sized and larger particles partly decouple from the gas and drift toward the star near the midplane. Outward transport would need to occur early, and primarily through the movement of small grains (Hughes & Armitage 2010).

The evolution of the disk structure will also play a role in the thermal history of grains and ices. Dust grains and their associated ices will be carried outward by the radial expansion of the disk, potentially moving grains from warm to colder regions. As the disk expands, material continues to fall onto it, and this could retain interstellar ice signatures. The resulting icy grains would therefore be a combination of warm material accreted earlier in the disk history with the colder, newer material. Also, young stars’ accretion rates generally decline with age, reducing their luminosity and thus the temperature at a given distance (Kenyon & Hartmann 1995).

Two recent papers have considered the effects of transport in disks on ice compositions. Price et al. (2021) were able to explain the exceptionally high CO/H₂O ratios observed in comets 2I/Borisov, C/2010 R2 (PanStarrs), and C/2009 P1 (Garradd) by inward drift of icy grains. As grains travel inward, they leave a region behind them that is depleted in water ice. Once inside of the CO snowline, the CO will desorb and the gas will be transported outward where it can recondense in the water-ice-poor region, resulting in higher CO/H₂O ice abundance ratios. Similar results have been found by Meijerink et al. (2009) and Ros & Johansen (2013).

Bergner & Ciesla (2021) traced the evolution of ices on grains as they are transported in a disk. They suggested pebbles formed at large radii drift inward to the comet formation region with their ices preserved, so that comets form from material formed or processed at large radii. Their model includes photoprocessing of ices at >100 au, something that is not considered in our work and that can lead to conversion of simple ice molecules into more complex ones.

Here we have focused here on midplane chemistry, but we do not model dynamics. Our toy model discusses combining CO-rich and CO-poor material in the midplane, which could be achieved by radial transport of grains, or by expansion of the disk and the corresponding change in physical conditions. Another plausible way of achieving this is mixing in the vertical direction. Since the temperature increases with height above the midplane, there is also a snowline some distance above the midplane (Figure 9), and material mixed upward will undergo thermal processing in the same way as midplane material does as the radius decreases. Ices that have been moved vertically will also be subject to an increased radiation field, further altering their chemistry. Grains fall toward the midplane where they coagulate to form larger solids, removing dust and volatile molecules from the disks upper layers (Krijt et al. 2016). However, disks observed today generally show some dust in their upper layers (Natta et al. 2007). Sustaining this distribution

likely requires collisional fragmentation of bigger solid bodies and upward transport of the next generation of dust.

The works of Price et al. (2021) and Bergner & Ciesla (2021) also provide potential mechanisms for combining CO-rich and CO-poor ices. Inflow of grains followed by evaporation of volatiles at their snowlines, and their outward transport in the gas, could enhance the abundances of molecules such as CO and CH₄ in ices at larger radii. Similarly, if less volatile species such as HCN behave in a similar way to H₂O, then the abundance of these molecules could be reduced at large radii. Price et al. (2021) only considered CO and H₂O, and it is not clear how this process can affect the abundances of other species in the ices. The photoprocessing of ices in the outer disk as discussed by Bergner & Ciesla (2021) and the formation and inflow of pebbles from this region to the comet formation region will also lead to changes in the ice abundance ratios.

These papers show that there is a complex interplay between chemistry and dynamics in disks that is still not fully explored. Price et al. (2021) only considered CO and H₂O and were specifically looking to account for very high CO/H₂O ratios. Might this scenario also be able to account for the range of observations of all molecules in other comets? The more-volatile species such as CH₄ might be expected to follow the behavior of CO and be enhanced in some regions of the disk as a result of transport in the gas from inside of their snowline to regions where the water ice is depleted. And less volatile molecules such as HCN may follow the behavior of water, being transported on grains inward and leaving behind a region where their abundance is reduced. The inclusion of outer disk photoprocessing of grains by Bergner & Ciesla (2021) could also provide a way to generate the observed range of molecular abundance ratios, with formation of more complex molecules out of simpler ones changing the abundances.

The important point here is that the models suggest that a combination of CO-rich (cold) and CO-poor (warm) ices is required to account for comet compositions. How this occurs is still unclear—the interplay of chemistry and transport is clearly very complex and still not well understood. In practice, it is likely that many processes affect the composition of cometary ices, including radial and vertical transport of small grains, as well as inward movement of larger pebbles. A further more detailed model is required to assess how these processes led to the variety of comet compositions seen in the solar system.

9.2. Comparison to the Eistруп Model

The χ^2 tests in Section 8.1 suggest that the best way to fit the comet observations by a model at a single location and time is for them to be assembled near the CO snowline. Comet compositions were also linked to the CO snowline by Eistруп et al. (2019), who used a maximum-likelihood function to determine where their model disks best fit measurements of individual comets. Their best fits roughly track the location of the CO snowline, but they found that the “reset” model was a better fit to the observations than the “inheritance” model (the E19 “inheritance” model is equivalent to our fiducial model).

While an exact comparison between the two models and their reaction networks has not been made, the differences are likely to originate in two factors. First, our model does not include the evolution of the disk and changes in the radial distribution of density and temperature, and the corresponding movement in the location of the icelines is likely to have an effect on the chemistry. The E19 CO snowline moved inward

with time, from about 28 au at 1 Myr to 12 au at 8 Myr. This cooling will affect the abundance of the more-volatile species such as CO and N₂ because they will condense at progressively smaller radii as the disk evolves.

Second, there are differences in the grain chemistry. Both E19 and our current work use a two-phase rate equation model, but there are differences in the way that the grain chemistry is treated. For example, a key parameter is the ratio of the barrier to diffusion (E_D) to the binding energy (E_b). E19 assume a ratio of 0.5, whereas we use 0.34. Both values are within the range suggested by the Monte Carlo simulations of Karssemeijer & Cuppen (2014). Our value was chosen to provide a reasonable match between our models and the observations of ices in molecular clouds (see Table 4). The slightly higher value in this work will slow down the rate at which grain reactions can occur. Another difference is in the number of active layers assumed. Here we choose four, whereas E19 have two. Again, this will make a difference to the reaction rates. There may also be differences in the grain reactions included and activation barriers assumed in the two models.

These differences in the model assumptions result in differences in the predicted mixing ratios. Comparing our Figure 4 with the “reset” model in Appendix A of E19, we can see both similarities and differences. The maximum CO/H₂O ratio in the E19 model is 1%, similar to the value we find over much of the disk, and well below the highest observed values of >20% in their comet sample. In their model, the CO appears to have been converted into H₂CO and CH₃OH, whereas these molecules are under-produced in the current work, with CO being processed into CO₂, HNCO, and OCS. These differences are likely due to differences in the grain chemical networks.

Both E19’s “reset” and “inheritance” models have similar CH₄ distributions, which in turn are similar to ours. The best matches to the observed abundances for all of the models are around the CH₄ snowline. Outside of this, the abundance relative to water is higher than observed.

For the hydrocarbons, E19’s “reset” and “inheritance” models produce quite different distributions. C₂H₂ is only produced in the “reset” model between 5 and 10 au and then only at high enough abundances to match the observations at times earlier than 2 Myr. The C₂H₂ in our “reset” model also peaks between 5 and 10 au, like E19’s but with smaller mixing ratios.

C₂H₆ is more widespread than C₂H₂ in both of E19s models and can be >10% relative to water in some parts of the disk. Their “reset” model provides a match to the range of observations on either side of the CO snowline, as does ours.

The observed HCN ratio in comets is <0.5% relative to H₂O. In our fiducial model, this only occurs near the HCN snowline, but can be achieved at larger radii in our “reset” model. The E19 “inheritance” model finds similar mixing ratios (HCN/H₂O \sim 1% between 5 and 10 au—a wider radius range than in our model) and also outside of the iceline, where our abundance is much higher. However, for their “reset” model, HCN/H₂O is greater than 10% everywhere in the disk, much higher than the observed value.

E19’s “reset” model produces considerably more OCS than their “inheritance” model. Both models cover the observed range of abundances in the region of the CO iceline. Our fiducial model differs, in that the OCS abundances are best fit by models outside of 20 au and at late times (>10 Myr), or near the OCS iceline. In our “reset” model, OCS only matches the

observations near its snowline. For the rest of the parameter space, our model over-produces OCS.

In summary, the differences between our model and that of E19 are likely to lie in differences in the details of the grain chemistry.

10. Conclusions

Our conclusions can be summarized as follows:

1. The range of comet compositions can only be matched if interstellar ices are retained. Starting the disk chemistry with “reset” abundances does not provide a way to account for the composition of the observed comets. Note: a hybrid model where some, but not all, of the interstellar ices are retained could provide a means of accounting for the observations but is not explored here.
2. The location and times at which models can match the range of mixing ratios observed for individual molecules do not overlap. No single place or time can account for the overall composition of any individual comet, nor for the average composition of the comet families.
3. Transport has a major role to play in explaining comet volatile compositions. Warm (CO-poor) and cold (CO-rich) material must be combined to account for the mean abundances of the observed JFCs and OCCs. The combination could be made by either radial or vertical transport along the disks’ temperature gradients.
4. Comparison of the models to the average Jupiter-family and OCC compositions suggests that the families formed in (at least) partly overlapping regions of the disk. Thus, independent conclusions from disk chemistry (this work) and the dynamical models of the early solar system (based on the Nice model) are consistent. However, the observations to date suggest that JFCs contain less CO than OCCs. If this difference is related to formation processes, our models suggest that the Jupiter-family group comprises more warmer material than OCCs. More definitive interpretation is pending an increased sample of CO detections in JFCs.
5. Abundances of individual comets may be more affected by post-formative processes than the ensemble properties (compositional ranges and average). Nevertheless, a combination of warm (CO-poor) and cold (CO-rich) material also accounts for the observed composition of eight individual comets.

None of the combined models presented here should be taken as exact descriptions of where or when the comets formed. Rather, they show that ices from different places in the protosolar nebula are required to produce compositions similar to those of comets. A single location and time is not sufficient to explain the abundances. The next logical steps in modeling involve understanding the effect of the mixing on the evolution of ice chemistry in PPDs.

Comets assembled out of materials processed for different lengths of time or in different regions of the disk would complicate constraining the location and epoch of formation solely through remote observations. If comets were assembled over a period of time, then solid particles’ history of growth and transport would have played a key role in determining the composition of the ices incorporated. As grains coagulated into bigger bodies, the ices deep inside would have become shielded from photons and cosmic rays and thus less likely to

suffer alteration. These issues could be explored using models combining the chemistry with the transport of gas and dust and the growth and fragmentation of solid particles. If comet nuclei contain chemically distinct components at the scale of boulders, pebbles, or grains, then determining their individual compositions to infer the conditions under which the components formed might require in situ measurements or even sample return.

The disk modeling research presented in this paper was conducted at the Jet Propulsion Laboratory, California Institute of Technology, under contract with the National Aeronautics and Space Administration and with the support of NASA’s Emerging Worlds Program award No. 15-EW15-2-0150 (Willacy, Turner). Integration with comet observations was also supported by NASA EW80NSSC20K0341 (Dello Russo, Vervack), and NSF AST-2009398 (Bonev) and AST-2009910 (Gibb). The project developed out of workshops on “Exploring the Early Solar System by Connecting Comet Composition and Protoplanetary Disk Models,” held in 2016 and 2018 at the International Space Science Institute, Bern. Some kinetic data used in this paper have been downloaded from the online database KIDA (Wakelam et al. 2012, <http://kida.obs.u-bordeaux1.fr>). © 2022. All rights reserved.

Appendix A Reactions Included from the KIDA Database

Table A1
Neutral–neutral Reactions Added to the UMIST RATE12 Database (McElroy et al. 2013) from the KIDA Database (Wakelam et al. 2012)

Reaction	f_j	α_j	β_j
O + CCS = CO + CS	1.00×10^{-10}		
H + CH ₃ CH ₃ = H ₂ + C ₂ H ₅	1.22×10^{-11}	1.5	3720.0
CH ₂ + CH ₃ CH ₃ = CH ₃ + C ₂ H ₅	1.07×10^{-11}	0.0	3980.0
CH ₂ + CH ₃ CH ₃ = CH ₄ + C ₂ H ₄	1.82×10^{-16}	6.0	3040.0
CH ₃ + CH ₃ CCH = C ₂ H ₅ + CH ₃ CH ₃	8.32×10^{-13}	0.0	4430.0
C ₂ H + CH ₃ CH ₃ = C ₂ H ₂ + C ₂ H ₅	5.10×10^{-11}	0.0	76.0
C ₂ H ₃ + C ₂ H ₅ = C ₂ H ₂ + CH ₃ CH ₃	9.80×10^{-12}		
C ₂ H ₃ + CH ₃ CH ₃ = C ₂ H ₄ + C ₂ H ₅	1.49×10^{-13}	3.3	5280.0
H ₂ + C ₂ H ₅ = H + CH ₃ CH ₃	4.23×10^{-15}	3.6	4250.0
CH ₄ + C ₂ H ₅ = CH ₃ + CH ₃ CH ₃	2.57×10^{-15}	4.14	6320.0
C ₂ H ₂ + C ₂ H ₅ = C ₂ H + CH ₃ CH ₃	4.50×10^{-13}	0.0	11800.0
C ₂ H ₄ + C ₂ H ₅ = C ₂ H ₃ + CH ₃ CH ₃	5.67×10^{-14}	3.13	9060.0
C ₂ H ₅ + C ₂ H ₅ = C ₂ H ₄ + CH ₃ CH ₃	2.40×10^{-12}		
H ₂ CCC + CH ₃ CH ₃ = CH ₂ CCH + C ₂ H ₅	1.90×10^{-10}		
CH ₂ CCH + CH ₃ CH ₃ = CH ₃ CCH + C ₂ H ₅	5.83×10^{-14}	3.3	9990.0
CH ₂ CCH + CH ₃ CH ₃ = C ₂ H ₅ + CH ₂ CCH ₂	5.83×10^{-14}	3.3	9990.0
NH + C ₂ H ₅ = N + CH ₃ CH ₃	4.00×10^{-11}		
H + C ₂ H ₅ = CH ₃ + CH ₃	1.25×10^{-10}		
H + C ₂ H ₅ = H ₂ + C ₂ H ₄	3.00×10^{-12}		
H + CH ₂ CCH ₂ = H + CH ₃ CCH	1.29×10^{-11}	0.0	1160.0
H + CH ₃ CHCH ₂ = CH ₃ + C ₂ H ₄	1.20×10^{-11}	0.0	655.0
CH ₂ + CH ₃ = H + C ₂ H ₄	7.00×10^{-11}		
CH ₂ + C ₂ H ₃ = C ₂ H ₂ + CH ₃	3.00×10^{-11}		
CH ₂ + C ₂ H ₅ = CH ₃ + C ₂ H ₄	3.00×10^{-11}		
CH ₃ + C ₂ H ₄ = C ₂ H ₃ + CH ₄	1.61×10^{-14}	3.7	4780.0
CH ₃ + C ₂ H ₅ = CH ₄ + C ₂ H ₄	1.90×10^{-12}		
CH ₃ + CH ₃ CH ₃ = CH ₄ + C ₂ H ₅	1.82×10^{-16}	6.0	3040.0
CH ₃ + CH ₂ CCH ₂ = C ₂ H ₂ + C ₂ H ₅	3.32×10^{-13}	0.0	4080.0
CCH + CH ₄ = C ₂ H ₂ + CH ₃	1.20×10^{-11}	0.0	491.0
CCH + CH ₃ CH ₃ = C ₂ H ₂ + C ₂ H ₅	5.10×10^{-11}	0.0	76.0
H ₂ + C ₂ H ₃ = H + C ₂ H ₄	3.01×10^{-20}		
C ₂ H ₃ + CH ₄ = CH ₃ + C ₂ H ₄	2.18×10^{-14}	4.02	2750.0
C ₂ H ₃ + C ₂ H ₃ = C ₂ H ₂ + C ₂ H ₄	3.50×10^{-11}		
H ₂ + H ₂ CCC = H + CH ₂ CCH	1.20×10^{-10}		
CH ₄ + H ₂ CCC = CH ₃ + CH ₂ CCH	5.90×10^{-11}		
C ₂ H ₃ + H ₂ CCC = C ₂ H ₂ + CH ₂ CCH	3.00×10^{-11}		
C ₂ H ₅ + H ₂ CCC = C ₂ H ₄ + CH ₂ CCH	1.50×10^{-11}		

Table A1
(Continued)

Reaction	f_j	α_j	β_j
$\text{CH}_4 + \text{CH}_2\text{CCH} = \text{CH}_3 + \text{CH}_3\text{CCH}$	1.74×10^{-14}	3.4	11700.0
$\text{CH}_4 + \text{CH}_2\text{CCH} = \text{CH}_3 + \text{CH}_2\text{CCH}_2$	1.74×10^{-14}	3.0	11700.0
$\text{N} + \text{CH}_3\text{CN} = \text{H} + \text{HCN} + \text{HCN}$	2.28×10^{-15}	0.0	813.0
$\text{NH} + \text{CH}_3 = \text{N} + \text{CH}_4$	4.00×10^{-11}		
$\text{NH} + \text{C}_2\text{H}_3 = \text{N} + \text{C}_2\text{H}_4$	4.00×10^{-11}		
$\text{NH}_2 + \text{C}_2\text{H}_4 = \text{NH}_3 + \text{C}_2\text{H}_3$	3.42×10^{-14}	0.0	1320.0
$\text{NH}_2 + \text{C}_2\text{H}_5 = \text{NH}_3 + \text{C}_2\text{H}_4$	4.15×10^{-11}		
$\text{NH}_2 + \text{CH}_3\text{CH}_3 = \text{NH}_3 + \text{C}_2\text{H}_5$	6.14×10^{-13}	0.0	3600.0
$\text{H} + \text{CH}_3\text{CN} = \text{HCN} + \text{CH}_3$	3.39×10^{-12}	0.0	3950.0
$\text{H} + \text{CH}_3\text{CN} = \text{CN} + \text{CH}_4$	1.66×10^{-13}	0.0	1500.0
$\text{O} + \text{CH}_3\text{CH}_3 = \text{OH} + \text{C}_2\text{H}_5$	8.63×10^{-12}	1.50	2920.0
$\text{OH} + \text{C}_2\text{H}_4 = \text{H}_2\text{O} + \text{C}_2\text{H}_3$	1.60×10^{-13}	2.74	2100.0
$\text{OH} + \text{CH}_3\text{CH}_3 = \text{H}_2\text{O} + \text{C}_2\text{H}_5$	6.90×10^{-12}	0.0	1010.0
$\text{CH}_2 + \text{H}_2\text{O} = \text{OH} + \text{CH}_3$	1.60×10^{-16}		
$\text{H}_2 + \text{HCO} = \text{H} + \text{H}_2\text{CO}$	2.70×10^{-13}	2.0	8980.0
$\text{HCO} + \text{CH}_4 = \text{CH}_3 + \text{H}_2\text{CO}$	1.39×10^{-13}	2.85	11300.0
$\text{HCO} + \text{C}_2\text{H}_3 = \text{CO} + \text{C}_2\text{H}_4$	1.50×10^{-10}		
$\text{HCO} + \text{C}_2\text{H}_5 = \text{CO} + \text{CH}_3\text{CH}_3$	2.01×10^{-10}		
$\text{HCO} + \text{CH}_3\text{CH}_3 = \text{H}_2\text{CO} + \text{C}_2\text{H}_5$	4.26×10^{-13}	2.72	9280.0
$\text{H}_2\text{O} + \text{HCO} = \text{OH} + \text{H}_2\text{CO}$	8.61×10^{-13}	1.35	13.1
$\text{HCN} + \text{HCO} = \text{CN} + \text{H}_2\text{CO}$	1.00×10^{-11}	0.0	17200.0
$\text{H}_2\text{CO} + \text{C}_2\text{H}_3 = \text{HCO} + \text{C}_2\text{H}_4$	8.22×10^{-14}	2.81	2950.0
$\text{H}_2\text{CO} + \text{C}_2\text{H}_5 = \text{HCO} + \text{CH}_3\text{CH}_3$	8.31×10^{-14}	2.81	2950.0
$\text{C} + \text{CO}_2 = \text{CO} + \text{CO}$	1.00×10^{-15}		
$\text{CCH} + \text{CCH} = \text{C}_2 + \text{C}_2\text{H}_2$	3.00×10^{-12}		
$\text{CCH} + \text{C}_2\text{H}_3 = \text{C}_2\text{H}_2 + \text{C}_2\text{H}_2$	1.600×10^{-12}		
$\text{C}_2\text{H} + \text{C}_2\text{H}_5 = \text{C}_2\text{H}_2 + \text{C}_2\text{H}_4$	3.00×10^{-12}		
$\text{CCH} + \text{C}_2\text{H}_5 = \text{CH}_3 + \text{CH}_2\text{CCH}$	3.00×10^{-11}		
$\text{NH}_2 + \text{C}_2\text{H}_2 = \text{C}_2\text{H} + \text{NH}_3$	1.11×10^{-13}		
$\text{CH}_4 + \text{C}_3\text{H} = \text{CH}_3 + \text{H}_2\text{CCC}$	1.2×10^{-11}		
$\text{OH} + \text{C}_2\text{H} = \text{O} + \text{C}_2\text{H}_2$	3.00×10^{-11}		
$\text{OH} + \text{C}_2\text{H} = \text{CO} + \text{CH}_2$	3.01×10^{-11}		
$\text{C}_2\text{H} + \text{HCO} = \text{CO} + \text{C}_2\text{H}_2$	1.00×10^{-10}		
$\text{C} + \text{H}_2\text{S} = \text{H} + \text{HCS}$	2.50×10^{-10}		
$\text{C} + \text{H}_3\text{S}^+ = \text{H}_2\text{S} + \text{C} + \text{H}$	7.51×10^{-8}	-0.50	

Table A1
(Continued)

Reaction	f_j	α_j	β_j
$\text{C} + \text{H}_2\text{CS} = \text{CS} + \text{CH}_2$	1.00×10^{-10}		
$\text{H}_3\text{CS}^+ + \text{e}^- = \text{H}_2\text{S} + \text{C} + \text{H}$	7.51×10^{-8}	-0.50	
$\text{S} + \text{C}_3\text{H} = \text{C}_2\text{H} + \text{CS}$	7.00×10^{-11}		
$\text{S} + \text{C}_3\text{H} = \text{C}_3\text{S} + \text{H}$	3.00×10^{-11}		
$\text{H} + \text{HSO}^+ = \text{SO}^+ + \text{H}_2$	2.00×10^{-10}		
$\text{H}_2 + \text{C}_3\text{S}^+ = \text{H} + \text{HC}_3\text{S}^+$	4.30×10^{-10}		
$\text{C}^+ + \text{C}_3\text{S} = \text{C}_3 + \text{CS}$	5.00×10^{-10}	-0.50	
$\text{C}^+ + \text{C}_3\text{S} = \text{C}_3 + \text{CS}^+$	5.00×10^{-10}	-0.50	
$\text{C} + \text{NS}^+ = \text{CN} + \text{S}^+$	6.00×10^{-10}		
$\text{C} + \text{SO}^+ = \text{CO} + \text{S}^+$	6.00×10^{-10}		
$\text{C} + \text{HCS} = \text{H} + \text{C}_2\text{S}$	2.00×10^{-10}		
$\text{C} + \text{HCS} = \text{S} + \text{C}_2\text{H}$	1.00×10^{-10}		
$\text{C} + \text{C}_2\text{S} = \text{C}_2 + \text{CS}$	2.00×10^{-10}		
$\text{C} + \text{C}_3\text{S} = \text{C}_3 + \text{CS}$	3.00×10^{-10}		
$\text{CH} + \text{CS} = \text{C}_2\text{S} + \text{H}$	1.50×10^{-10}		
$\text{CH} + \text{CS} = \text{C}_2\text{H} + \text{S}$	5.00×10^{-11}		
$\text{CH} + \text{C}_3\text{S} = \text{CS} + \text{C}_3\text{H}$	1.00×10^{-10}		
$\text{CH}_3^+ + \text{CS} = \text{CH}_3\text{CS}^+ + \text{PHOTON}$	1.00×10^{-13}	-1.00	0.0
$\text{N} + \text{NS}^+ = \text{N}_2 + \text{S}^+$	6.00×10^{-10}		
$\text{N} + \text{C}_2\text{S} = \text{CN} + \text{CS}$	3.00×10^{-11}	0.17	
$\text{NH} + \text{CS} = \text{HNC} + \text{S}$	1.00×10^{-11}	0.0	1200.0
$\text{NH} + \text{C}_2\text{S} = \text{HCN} + \text{CS}$	2.00×10^{-11}		
$\text{NH} + \text{C}_2\text{S} = \text{HNC} + \text{CS}$	2.00×10^{-11}		
$\text{O} + \text{C}_3\text{S} = \text{CO} + \text{C}_2\text{S}$	1.94×10^{-11}	0.0	231.0
$\text{S} + \text{C}_2\text{H}_3 = \text{CH}_3 + \text{CS}$	4.00×10^{-11}		
$\text{S} + \text{C}_2\text{H}_3 = \text{HS} + \text{C}_2\text{H}_2$	1.00×10^{-11}		
$\text{S} + \text{C}_3\text{H}_2 = \text{C}_2\text{H}_2 + \text{CS}$	1.00×10^{-10}		
$\text{S} + \text{C}_2\text{S} = \text{CS} + \text{CS}$	1.00×10^{-10}		
$\text{H}_2\text{S}^+ + \text{HNC} = \text{HCNH}^+ + \text{HS}$	8.97×10^{-10}	-0.50	
$\text{H}_2\text{S}^+ + \text{HCN} = \text{HCNH}^+ + \text{HS}$	9.46×10^{-10}	-0.50	
$\text{HSO}^+ + \text{CO} = \text{HCO}^+ + \text{SO}$	1.00×10^{-9}		
$\text{HSO}^+ + \text{H}_2\text{O} = \text{SO} + \text{H}_3\text{O}^+$	2.00×10^{-9}		

Note. Rates are given by the Arrhenius equation $k_j = f_j (T/300.)^{\alpha_j} \exp(-\beta_j/T) \text{ cm}^{-3} \text{ s}^{-1}$.

Appendix B

Comet Observations

Comet observations used in this paper. Data are from [DR16](#) and Saki et al. (2020).

Table B1
Observational Data Used in This Paper

Comet	Family	CH ₃ OH	HCN	NH ₃	H ₂ CO	C ₂ H ₂	C ₂ H ₆	CH ₄	CO	OCS
2P/Encke	JFC	3.48	0.09	...	<0.13	<0.08	0.31	0.34	<1.77	0.06
6P/d'Arrest	JFC	2.8	0.03	0.52	0.36	<0.05	0.29
9P/Tempel 1	JFC	1.4	0.2	0.9	0.84	0.13	0.29	0.54	4.3	...
10P/Tempel 2	JFC	1.58	0.13	0.83	<0.11	<0.07	0.39
21P/G-Z	JFC	1.22	<0.27	...	(<0.8)	<0.42	0.12	...	2.2	0.1
73P/SW3-B	JFC	0.54	0.29	<0.09	0.14	0.03	0.17	(<4.1)	(<19)	...
73P/SW3-C	JFC	(0.49)	(0.22)	(<0.16)	(0.12)	(0.03)	(0.11)	<0.25	0.53	...
81P/Wild 2	JFC	0.9	0.27	0.6	0.22	0.15	0.45
103P/Hartley 2	JFC	1.95	0.24	0.66	0.13	0.10	0.75	<0.47	0.3	...
8P/Tuttle	OCC	2.0	0.07	...	<0.04	0.04	0.26	0.37	0.4	...
153P/Ikeya-Zhang	OCC	2.9	0.21	...	0.83	0.21	0.57	0.5	5.7	...
C/1995 O1 (Hale-Bopp)	OCC	...	0.36	0.28	0.62	1.22	26.2	0.4
C 1996 B2 (Hyakutake)	OCC	...	0.19	0.20	0.61	0.95	18.2	0.2
C/1999 H1 (Lee)	OCC	1.9	0.22	0.7	0.7	0.25	0.63	1.22	1.6	<3.6
C/1999 S4 (LINEAR)	OCC	<0.2	0.09	<0.13	0.09	0.15	0.58	<3.6
C/1999 T1 (McNaught-Hartley)	OCC	1.7	0.37	0.65	1.4	17	...
C/2000 WM ₁ (LINEAR)	OCC	0.95	0.14	...	0.2	<0.05	0.47	0.35	0.48	...
C/2001 A2 (LINEAR)	OCC	2.97	0.47	...	0.15	0.37	1.6	1.48	3.9	...
C/2002 T7 (LINEAR)	OCC	3.4	0.79	1.9	0.04
C/2003 K4 (LINEAR)	OCC	1.83	0.07	<0.55	<0.07	<0.04	0.41	0.86
C/2004 Q2 (Machholz)	OCC	1.52	0.15	0.31	0.16	0.07	0.54	1.37	5.07	...
C/2006 M4 (SWAN)	OCC	3.28	0.49	0.82	0.5	...
C/2006 P1 (McNaught)	OCC	...	0.24	1.5	0.49	0.45	0.47	0.42	1.8	...
C/2007 N1 (Lulin)	OCC	3.72	0.14	0.24	0.12	0.07	0.68	1.19	2.18	...
C/2007 W1 (Boattini)	OCC	3.69	0.5	1.74	<0.12	0.29	1.97	1.57	4.50	...
C/2009 P1 (Garradd)	OCC	2.74	0.25	0.48	0.09	0.07	0.82	0.95	8.9	<0.2
C/2012 F6 (Lemmon) ^a	OCC	1.48	0.19	0.52	<0.12	<0.05	0.29
C/2012 F6 (Lemmon) ^b	OCC	0.54	0.67	4.03	...
C/2012 S1 (ISON) ^c	OCC	1.13	0.07	<0.95	0.16	0.11	0.27	0.32	1.37	0.16
C/2012 S1 (ISON) ^d	OCC	...	0.28	3.63	1.1	0.24
C/2013 R1 (Lovejoy)	OCC	2.29	0.25	0.1	<0.06	<0.07	0.59	0.92	11.3	0.034

Note. Abundances are given as percentages with respect to H₂O. Abundances in parentheses were not used by [DR16](#) to determine the average comet compositions given in Table 5. [DR16](#) also discuss 17P/Holmes and C/2010 G2 but these are not included in this table because they were not used to calculate the average molecular mixing ratios. Also shown are the OCS abundances from Saki et al. (2020).

References. ^a Measurements at $R_b > 1.2$ au, ^b Measurements at $R_b = 0.75$ au, ^c Measurements at $R_b > 0.83$ au, ^d Measurements at $R_b < 0.59$ au.

Appendix C

The New Compilation of Comet Compositions from Lippi et al. (2020, 2021)

While this paper was in review, Lippi et al. (2020, 2021) hereafter [L20/L21](#) published an important reanalysis of the composition of 20 comets, including all of those from the [DR16](#) sample to which we compare our disk model outputs. The same eight molecules were considered as were included in the [DR16](#) survey. [L20/L21](#) applied fluorescence models to interpret cometary emission and telluric transmittance models accounting for attenuation in the Earth's atmosphere, which have been substantially improved since about 2010 (Villanueva et al. 2013, and references therein). The [DR16](#) survey summarized work since the early stages of infrared high-resolution observation of comets in the 1990s, so we carefully assessed how the new [L20/L21](#) results affect our analyses and conclusions.

The main conclusions from our work (Conclusions 1–4 in Section 10) are based on ensemble properties of comets: average abundances and abundance ranges for individual molecules among the studied comets. These conclusions are not affected by the new survey because it results in differences between measurements in individual comets, but similar ranges and averages in abundances. [L20/L21](#) report median values, very similar to the average abundances from [DR16](#) for HCN, NH₃, C₂H₂, C₂H₆, and CH₄, and sufficiently close for CH₃OH, thereby not affecting Conclusions 1–4 from this paper. The larger difference in CO (5.2+/-1.3 from [DR16](#) versus abundance median of 2.66 in [L21](#)) is strongly dependent on sample size because the CO/H₂O relative abundance varies three orders of magnitude among comets.

The last conclusion (No. 5) in our work is based on comparison between disk model outputs and measurements in the individual comets listed Table 7: 103P/Hartley 2, 9p/Tempel 1, C/1999 H1 (Lee), C/2009 P1 (Garradd), C/2013 R1 (Lovejoy), C/2007 N1 (Lulin), C/2012 S1 (ISON), and C/2004 Q2 (Machholz). We therefore applied a χ^2 test to the measurements from [L20/L21](#) (Table C1). These do not alter our conclusions that combining CO-rich and CO-poor material is required to reproduce comet abundances, and that dynamics (mixing hot and cold material) plays a key role in determining the chemistry.

Table C1





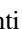
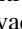

Best-fit Parameters to the [L20/L21](#) Data Assuming Comets Are Made from Material from Two Radii in the Fiducial Model, One Inside (R_1) and One Outside (R_2) the Snowline

Comet	Time	R_1 (%)	R_2 (%)	χ^2
9P/Tempel 1	1.6	4 (95%)	19 (5%)	0.92
103P/Hartley 2	1.6	4 (90%)	17 (10%)	0.76
C/1999 H2 (Lee)	1.6	4 (90%)	18 (10%)	2.36
C/2004 Q2 (Machholz)	2.0	4 (85%)	20 (15%)	3.38
C/2007 N1 (Lulin)	2.0	3 (85%)	19 (15%)	2.20
C/2009 P1 (Garradd)	2.0	3 (70%)	20 (30%)	7.3
C/2012 S1 (ISON)	2.0	4 (90%)	18 (10%)	3.57
C/2013 R1 (Lovejoy)	2.0	3 (75%)	21 (25%)	6.2

Note. Shown are the combinations of R_1 and R_2 with the lowest χ^2 that also match the observed abundances of each molecule to within a factor of 10. The contribution of each radius is given as a percentage of the total calculated composition (so percentage of R_1 given is $100 \times f_{R1}$ where f_{R1} is the fraction of R_1 in Equation (8)). The composition of all of our comet sample can be matched by such combined models.

The reason that our conclusions even on individual comets included in our study hold is plausibly explained by comparing [DR16](#) and [L20/L21](#) results. While significant differences are present for some molecules, most notably H₂CO, for each comet in Table 11, abundances of four or more molecules (out of eight) either agree within reported uncertainties, or are sufficiently close, to not affect our Conclusion 5. Comet C/2007 N1 has the best agreement: virtually all species, but even comets analyzed much earlier (C/1999 H1 and 9P), show similarities in at least half the measured abundances.

ORCID iDs

Karen Willacy  <https://orcid.org/0000-0001-6124-5974>
 Neal Turner  <https://orcid.org/0000-0001-8292-1943>
 Boncho Bonev  <https://orcid.org/0000-0002-6391-4817>
 Erika Gibb  <https://orcid.org/0000-0003-0142-5265>
 Neil Dello Russo  <https://orcid.org/0000-0002-8379-7304>
 Michael DiSanti  <https://orcid.org/0000-0001-8843-7511>
 Ronald J. Vervack Jr.  <https://orcid.org/0000-0002-8227-9564>
 Nathan X. Roth  <https://orcid.org/0000-0002-6006-9574>

References

- A'Hearn, M. F. 2017, [RSPTA](#), **375**, 20160261
 A'Hearn, M. F., Feaga, L. M., Keller, H. U., et al. 2012, [ApJ](#), **758**, 29
 A'Hearn, M. F., Millis, R. C., Schleicher, D. O., Osip, D. J., & Birch, P. V. 1995, [Icar](#), **118**, 223
 Bergin, E. A., Aikawa, Y., Blake, G. A., & van Dishoeck, E. F. 2007, in *Protostars and Planets V*, ed. B. Reipurth, D. Jewitt, & K. Keil (Tucson, AZ: Univ. Arizona Press), 751
 Bergner, J. B., & Ciesla, F. 2021, [ApJ](#), **919**, 45
 Bonev, B. P., Willacy, K., Mumma, M. J., et al. 2014, AAS/Division for Planetary Sciences Meeting, **46**, 209.18
 Boogert, A. C. A., Gerakines, P. A., & Whittet, D. C. B. 2015, [ARA&A](#), **53**, 541
 Bregman, J. D., Witteborn, F. C., Allamandola, L. J., et al. 1987, [A&A](#), **187**, 616
 Brownlee, D. E., Joswiak, D., Matrajt, G., & Tsou, P. 2009, in *ASP Conf. Ser.*, **414**, Cosmic Dust—Near and Far, ed. T. Henning, E. Grün, & J. Steinacker (San Francisco, CA: ASP), 157
 Castillo-Rogez, J., Johnson, T. V., Lee, M. H., et al. 2009, [Icar](#), **204**, 658
 Cleeves, L. I., Adams, F. C., & Bergin, E. A. 2013, [ApJ](#), **772**, 5
 Crovisier, J., Brooke, T. Y., Hanner, M. S., et al. 1996, [A&A](#), **315**, L385
 Cuppen, H. M., Walsh, C., Lamberts, T., et al. 2017, [SSRv](#), **212**, 1
 d'Alessio, P., Calvet, N., & Harman, L. 2001, [ApJ](#), **553**, 321
 Davidsson, B. J. R., Sierks, H., Güttler, C., et al. 2016, [A&A](#), **592**, A63
 Dello Russo, N., Kawakita, H., Vervack, R. J., & Weaver, H. A. 2016, [Icar](#), **278**, 301
 Dello Russo, N., Vervack, R. J., Weaver, H. A., et al. 2007, [Natur](#), **448**, 172
 DiSanti, M. A., Bonev, B. P., Russo, N. D., et al. 2017, [AJ](#), **154**, 246
 DiSanti, M. A., Mumma, M. J., Dello Russo, N., et al. 1999, [Natur](#), **399**, 662
 Donn, B. D. 1990, [A&A](#), **235**, 441
 Drozdovskaya, M. N., Walsh, C., van Dishoeck, E. F., et al. 2016, [MNRAS](#), **462**, 977
 Drozdovskaya, M. N., Walsh, C., Visser, R., Harsono, D., & van Dishoeck, E. F. 2014, [MNRAS](#), **445**, 913
 Eistrup, C., Walsh, C., & van Dishoeck, E. F. 2019, [A&A](#), **629**, A84
 Furuya, K., & Aikawa, Y. 2014, [ApJ](#), **790**, 97
 Gibb, E., Bonev, B. P., Willacy, K., et al. 2017, *Asteroids, Comets and Meteors (ACM2017)* (Montevideo, Uruguay), 307
 Gladman, B. 2005, [Sci](#), **307**, 71
 Gomes, R., Levison, H. F., Tsiganis, K., & Morbidelli, A. 2005, [Natur](#), **435**, 466
 Guilbert-Lepoutre, A., Rosenberg, E. D., Prialnik, D., & Besse, S. 2016, [MNRAS](#), **462**, S146
 Hughes, A. L. H., & Armitage, P. J. 2010, [ApJ](#), **719**, 1633
 Indriolo, N., Geballe, T. R., Oka, T., & McCall, B. J. 2007, [ApJ](#), **671**, 1736
 Kamp, I. 2020, [IAUS](#), **345**, 115
 Karssemeijer, L. J., & Cuppen, H. M. 2014, [A&A](#), **569**, A107
 Kataoka, A., Tanaka, H., Okuzumi, S., & Wada, K. 2013, [A&A](#), **557**, L4

- Kemper, F., Vriend, W. J., & Tielens, A. G. G. M. 2004, *ApJ*, **609**, 826
- Kenyon, S. J., & Hartmann, L. 1995, *ApJS*, **101**, 117
- Krijt, S., Ciesla, F. J., & Bergin, E. A. 2016, *ApJ*, **833**, 285
- Lauck, T., Karssemeijer, L., Shulenberger, K., et al. 2015, *ApJ*, **801**, 118
- Lippi, M., Villanueva, G. L., Mumma, M. J., et al. 2020, *AJ*, **159**, 157
- Lippi, M., Villanueva, G. L., Mumma, M. J., & Faggi, S. 2021, *AJ*, **162**, 74
- Lunine, J. I., Engel, S., Rizk, B., & Horanyi, M. 1991, *Icar*, **94**, 333
- McCall, B. J., Huneycutt, A. J., Saykally, R. J., et al. 2003, *Natur*, **422**, 500
- McElroy, D., Walsh, C., Markwick, A. J., et al. 2013, *A&A*, **550**, A36
- Meijerink, R., Pontoppidan, K. M., Blake, G. A., Poelman, D. R., & Dullemond, C. P. 2009, *ApJ*, **704**, 1471
- Mousis, O., Gautier, D., Bockelée-Morvan, D., et al. 2000, *Icar*, **148**, 513
- Natta, A., Testi, L., Calvet, N., et al. 2007, in *Protostars and Planets V*, ed. B. Reipurth, D. Jewitt, & K. Keil (Tuscon, AZ: Univ. Arizona Press), 767
- Neufeld, D. A., & Hollenbach, D. J. 1994, *ApJ*, **428**, 170
- Oort, J. H. 1950, *BAN*, **11**, 91
- Penteado, E. M., Walsh, C., & Cuppen, H. M. 2017, *ApJ*, **844**, 71
- Prasad, S. S., & Tarafdar, S. P. 1983, *ApJ*, **267**, 603
- Price, E. M., Cleeves, L. I., Bodewits, D., & Öberg, K. I. 2021, *ApJ*, **913**, 9
- Rickman, H. 2010, in *Lecture Notes in Physics*, Vol. 790 ed. J. Souchay & R. Dvorak (Berlin: Springer), 341
- Ros, K., & Johansen, A. 2013, *A&A*, **552**, A137
- Rubin, M., Altwegg, K., Balsiger, H., et al. 2015, *Sci*, **348**, 232
- Rubin, M., Altwegg, K., Balsiger, H., et al. 2019, *MNRAS*, **489**, 594
- Ruffle, D. P., & Herbst, E. 2001, *MNRAS*, **322**, 770
- Saki, M., Gibb, E. L., Bonev, B. P., et al. 2020, *AJ*, **160**, 184
- Seifert, R. A., Cleeves, L. I., Adams, F. C., & Li, Z. Y. 2021, *ApJ*, **912**, 136
- Semenov, D., Wiebe, D., & Henning, T. 2004, *A&A*, **417**, 93
- Shakura, N. I., & Sunyaev, R. A. 1973, *A&A*, **24**, 337
- Simon, J. B., Armitage, P. J., Li, R., & Youdin, A. N. 2016, *ApJ*, **822**, 55
- Snodgrass, C., & Jones, G. H. 2019, *NatCo*, **10**, 5418
- Testi, L., Birmstiel, T., Ricci, L., et al. 2014, in *Protostars and Planets VI*, ed. H. Beuther et al. (Tuscon, AZ: Univ. Arizona Press), 339
- Trinquier, A., Elliott, T., Ulfbeck, D., et al. 2009, *Sci*, **324**, 374
- Tsiganis, K., Gomes, R., Morbidelli, A., & Levison, H. F. 2005, *Natur*, **435**, 459
- Turner, N. J., Fromang, S., Gammie, C., et al. 2014, *Protostars and Planets VI* (Tuscon, AZ: Univ. Arizona Press), 411
- Turner, N. J., & Smith, G. H. 1999, *AJ*, **118**, 3039
- van Boekel, R., Min, M., Leinert, C., et al. 2004, *Natur*, **432**, 479
- Villanueva, G. L., Magee-Sauer, K., & Mumma, M. J. 2013, *JQSRT*, **129**, 158
- Visser, R., van Dishoeck, E. F., & Black, J. H. 2009, *A&A*, **503**, 323
- Wakelam, V., Herbst, E., Loison, J. C., et al. 2012, *ApJS*, **199**, 21
- Weidenschilling, S. J. 1977, *Ap&SS*, **51**, 153
- Weidenschilling, S. J. 1997, *Icar*, **127**, 290
- Willacy, K., Alexander, C., Ali-Dib, M., et al. 2015, *SSRv*, **197**, 151
- Yang, L., Ciesla, F. J., & Alexander, C. M. O. D. 2013, *Icar*, **226**, 256
- Youdin, A. N., & Goodman, J. 2005, *ApJ*, **620**, 459
- Zolensky, M. E., Zega, T. J., Yano, H., et al. 2006, *Sci*, **314**, 1735